

Alzheimer's disease risk gene CD2AP is a dose-sensitive determinant of synaptic structure and plasticity

Matea Pavešković^{1,2,3}, Ruth B. De-Paula^{2,3,4}, Shamsideen A. Ojelade^{2,3}, Evelyne K. Tantry^{5,6}, Mikhail Y. Kochukov^{2,5}, Suyang Bao^{2,6}, Surabi Veeraragavan^{2,5}, Alexandra R. Garza^{2,5}, Snigdha Srivastava^{2,5,7}, Si-Yuan Song^{1,2}, Masashi Fujita⁸, Duc M. Duong⁹, David A. Bennett¹⁰, Philip L. De Jager⁸, Nicholas T. Seyfried⁹, Mary E. Dickinson^{5,11}, Jason D. Heaney⁵, Benjamin R. Arenkiel^{1,2,5,†}, Joshua M. Shulman^{1,2,3,5,12,†,*}

¹Department of Neuroscience, Baylor College of Medicine, One Baylor Plaza, Houston, TX 77030, United States

²Jan and Dan Duncan Neurological Research Institute, Texas Children's Hospital, 1250 Moursund Street, Houston, TX 77030, United States

³Department of Neurology, Baylor College of Medicine, One Baylor Plaza, Houston, TX 77030, United States

⁴Quantitative and Computational Biology Program, Baylor College of Medicine, One Baylor Plaza, Houston, TX 77030, United States

⁵Department of Molecular and Human Genetics, Baylor College of Medicine, One Baylor Plaza, Houston, TX 77030, United States

⁶Development, Disease Models, and Therapeutics Graduate Program, Baylor College of Medicine, One Baylor Plaza, Houston, TX 77030, United States

⁷Medical Scientist Training Program, Baylor College of Medicine, One Baylor Plaza, Houston, TX 77030, United States

⁸Center for Translational and Computational Neuroimmunology, Department of Neurology and the Taub Institute for Research on Alzheimer's Disease and the Aging Brain, Columbia University Irving Medical Center, 630 West 168th Street, New York, NY, United States

⁹Departments of Biochemistry and Neurology, Emory University School of Medicine, 100 Woodruff Circle, Atlanta, GA 30322, United States

¹⁰Rush Alzheimer's Disease Center, Rush University Medical Center, 600 S. Paulina Street, Chicago, IL 60612, United States

¹¹Department of Molecular Physiology and Biophysics, Baylor College of Medicine, One Baylor Plaza, Houston, TX 77030, United States

¹²Center for Alzheimer's and Neurodegenerative Diseases, Baylor College of Medicine, One Baylor Plaza, Houston, TX 77030, United States

*Corresponding author. Jan and Dan Duncan Neurological Research Institute, Texas Children's Hospital, 1250 Moursund St., Suite N.1150, Houston, TX 77030, United States. E-mail: Joshua.Shulman@bcm.edu

†Benjamin R. Arenkiel and Joshua M. Shulman contributed equally, co-senior authors.

Abstract

CD2-Associated protein (CD2AP) is a candidate susceptibility gene for Alzheimer's disease, but its role in the mammalian central nervous system remains largely unknown. We show that CD2AP protein is broadly expressed in the adult mouse brain, including within cortical and hippocampal neurons, where it is detected at pre-synaptic terminals. Deletion of *Cd2ap* altered dendritic branching and spine density, and impaired ubiquitin-proteasome system activity. Moreover, in mice harboring either one or two copies of a germline *Cd2ap* null allele, we noted increased paired-pulse facilitation at hippocampal Schaffer-collateral synapses, consistent with a haploinsufficient requirement for pre-synaptic release. Whereas conditional *Cd2ap* knockout in the brain revealed no gross behavioral deficits in either 3.5- or 12-month-old mice, *Cd2ap* heterozygous mice demonstrated subtle impairments in discrimination learning using a touchscreen task. Based on unbiased proteomics, partial or complete loss of *Cd2ap* triggered perturbation of proteins with roles in protein folding, lipid metabolism, proteostasis, and synaptic function. Overall, our results reveal conserved, dose-sensitive requirements for CD2AP in the maintenance of neuronal structure and function, including synaptic homeostasis and plasticity, and inform our understanding of possible cell-type specific mechanisms in Alzheimer's Disease.

Keywords: Alzheimer's disease; synapse; CD2AP; proteomics; proteostasis; plasticity; haploinsufficiency; endocytosis; apolipoproteins; lipid metabolism

Introduction

Alzheimer's disease (AD) is an incurable neurodegenerative disorder with evidence for substantial heritability [1]. More than 70 AD susceptibility loci have been identified by human genome-wide association studies (GWAS), with hopes for new therapies targeting the proximate disease causes [2–4]. However, the translational path from GWAS faces two overarching challenges. First, susceptibility signals rarely definitively identify the responsible causal gene, instead highlighting a large genomic window with multiple candidates. Most common variants implicated by GWAS fall in noncoding regions and likely cause only modest changes in expression in one or more target genes [5].

The availability of human transcriptome references, including from brain, have significantly improved our ability to prioritize candidate causal genes [6]. A second obstacle arises since the majority of candidates have largely unknown functions, especially within the nervous system. Moreover, understanding neurodegeneration requires genetic analysis within the context of the aging, adult brain, ideally using pertinent functional outcomes, and differentiating potential roles within heterogeneous cell types, such as neuronal subtypes and glia.

AD is characterized clinically by the progressive loss of episodic memory and, pathologically, by synaptic and neuronal loss that begins in the CA1 region of the hippocampus [1, 7, 8]. While follow-up of AD susceptibility genes has begun to

Received: February 27, 2024. Revised: June 15, 2024

© The Author(s) 2024. Published by Oxford University Press.

This is an Open Access article distributed under the terms of the Creative Commons Attribution Non-Commercial License (<https://creativecommons.org/licenses/by-nc/4.0/>), which permits non-commercial re-use, distribution, and reproduction in any medium, provided the original work is properly cited. For commercial re-use, please contact journals.permissions@oup.com

strongly implicate microglial inflammation and lipid metabolism, comparatively few data have emerged on potential genetic determinants of synaptic and circuit vulnerability. We recently reported that the *Drosophila* homolog of the AD susceptibility gene, CD2-Associated Protein (CD2AP), is a regulator of synaptic transmission and proteostasis [9]. CD2AP encodes a 639-amino acid multifunctional adaptor protein, including a proline-rich region, three SH3 motifs, and an actin-binding domain [10, 11]. Before its identification as an AD risk locus [2–4, 12], loss-of-function mutations in CD2AP were identified as a rare, autosomal dominant cause of focal segmental glomerulosclerosis, likely due to a requirement for maintaining structural integrity of the slit diaphragm [13–15]. In mice, *Cd2ap*^{-/-} knockout from the germline recapitulates progressive renal failure, leading to death by approximately 7 weeks [16]. *Cd2ap*^{+/-} heterozygotes develop mild glomerular dysfunction by 9 months of age, consistent with a haploinsufficient requirement in the kidney [13]. In fact, *Cd2ap* is widely expressed in many tissues, including the brain [11, 17, 18]. Following transgenic rescue of expression in the kidney, mice lacking *Cd2ap* survived to adulthood with apparently normal behavior, but blood brain barrier integrity was compromised causing increased susceptibility to pharmacologically induced seizures [19]. In primary cultures derived from rat cerebellar granular neurons, *Cd2ap* knockdown disrupts neurite outgrowth [17], possibly due to roles in endocytosis and trafficking of key signaling factors [9, 10, 20–23]. Importantly, besides CD2AP, numerous other AD susceptibility gene candidates participate in endocytic pathways, which are known to regulate synaptic vesicle recycling and neurotransmission [24]. Additional work in cell culture, fruit fly, and mouse models has also suggested potential interactions between CD2AP and the amyloid-beta peptide or tau protein, which form AD amyloid plaque and neurofibrillary tangle pathologies [25–27].

In sum, the potential requirements of CD2AP in the adult brain remain incompletely explored, creating an important gap for understanding its role in disease. Here, we show that CD2AP is present at the mammalian synapse, where it likely regulates synaptic structure and function, and we also uncover evidence for a possible haploinsufficient requirement based on neurophysiology, behavior, and proteomics.

Results

***Cd2ap* is expressed ubiquitously in neurons throughout the mouse brain**

Using a new polyclonal anti-CD2AP antibody, we detected broad expression throughout the wildtype mouse brain (Fig. 1A). Antibody staining was largely absent in brain tissue from mice homozygous for a previously-characterized, germline *Cd2ap* knockout allele (*Cd2ap*^{-/-}) [16] (Fig. 1B and Fig. S1A). In further support of specificity, we detected an 80 kDa CD2AP protein band on Western blot from kidney homogenates as expected [11], where CD2AP is highly expressed [18, 28], and this band was absent from *Cd2ap*^{-/-} animals (Fig. S1B). Based on a comprehensive survey of coronal slices, *Cd2ap* appeared broadly expressed throughout the cortex, including the retrosplenial, motor, somatosensory, auditory, ectorhinal, perirhinal, entorhinal, and piriform areas. Expression appeared enriched within the hippocampus, where CD2AP was detected in the cornu ammonis (CA) 1, CA2, and CA3 regions and the dentate gyrus, including the hilus and polymorphic layer (Fig. 1A and C and Fig. S2) [29–31]. Positive staining was also noted in the thalamus, habenula, the amygdala, and other regions.

We confirmed that CD2AP protein is expressed in neurons based on co-staining with neuronal markers, including the cytoplasmic microtubule-associated protein 2 (MAP2), and NeuN, which predominantly labels neuronal nuclei [32] (Fig. 1C and Fig. S3A). At higher-power, CD2AP appeared localized within the cytoplasm in the soma of hippocampal and cortical neurons (Fig. 1D and Fig. S2A). CD2AP also colocalized with the pre-synaptic marker Synapsin (Fig. 1E and Fig. S2B). By comparison, we found comparatively poor overlap with the post-synaptic marker PSD-95 (Fig. 1E) [33, 34]. We also confirmed *Cd2ap* neuronal expression and pre-synaptic localization *in vitro* using wildtype primary cortical neurons (Fig. S3B). While CD2AP was not detectable within cultured astrocytes when co-staining for GFAP (Fig. S4), we cannot exclude low-level glial expression.

Based on a recently generated human brain single-nucleus expression atlas, CD2AP mRNA signal was reported within numerous neuronal subtypes as well as non-neuronal cells, including astrocytes, oligodendrocytes, endothelial cells, and microglia (Fig. S5A) [35]. Moreover, human GWAS studies suggest that AD risk variants at the CD2AP locus significantly alter gene expression [2, 3, 36]. We leveraged new paired single nucleus RNA-sequencing and whole genome sequencing from 424 human dorsolateral prefrontal cortex postmortem brain tissue samples in which expression quantitative trait loci (eQTL) have been mapped to specific cell types [6, 35]. This analysis confirmed that 3 established genome-wide significant risk variants for AD (rs7767350, rs9369716, rs9473117)—which are in strong linkage disequilibrium and therefore proxies for the same underlying susceptibility allele—increase expression of human CD2AP mRNA in both excitatory and inhibitory neurons, as well as microglia (Fig. S5B–D). By contrast, eQTLs were not apparent in astrocytes, oligodendrocytes, or endothelial cells. Together, these results support CD2AP as the responsible causal gene at this AD susceptibility locus and motivate our studies to elucidate requirements within the brain, including in neurons.

***Cd2ap* is required for synaptic proteostasis and dendritic morphology**

In *Drosophila*, loss-of-function in the human CD2AP gene ortholog disrupts proteasome function, leading to impaired turnover of synaptic proteins and aberrant neural transmission and plasticity [9]. To evaluate potential cell autonomous requirements in mammalian neurons, we performed CRISPR-mediated deletion of *Cd2ap* in primary mouse cortical neuron cultures. As expected, mammalian neurons lacking *Cd2ap* had significantly reduced proteasome activity, based on turnover of the proteasome substrate Suc-LLVY-AMC, along with increased expression of the pre- and post-synaptic proteins, Synapsin and PSD95, respectively, consistent with our prior findings (Fig. 2) [9]. In addition, *Cd2ap* KO neurons displayed decreased number of Sholl intersections, reduced dendritic branching, and increased dendritic spine density (Fig. 3A). With further analysis of spine morphology, we discovered increased density of filopodia and mushroom-shaped spines, which represent immature and more stable spines, respectively [37, 38] (Fig. 3B).

We also evaluated dendritic morphology *in vivo*, examining pyramidal neuron morphology in the hippocampal CA1 region from approximately 5-week-old mice homozygous or heterozygous for the *Cd2ap* germline knockout allele (Fig. 3C). Complete loss of *Cd2ap* resulted in decreased branching of basal dendrites from hippocampal neurons, while apical dendrites were unaffected (Fig. 3E). The number of dendritic Sholl intersections was unchanged in both apical and basal dendrites (Fig. S6). Further,

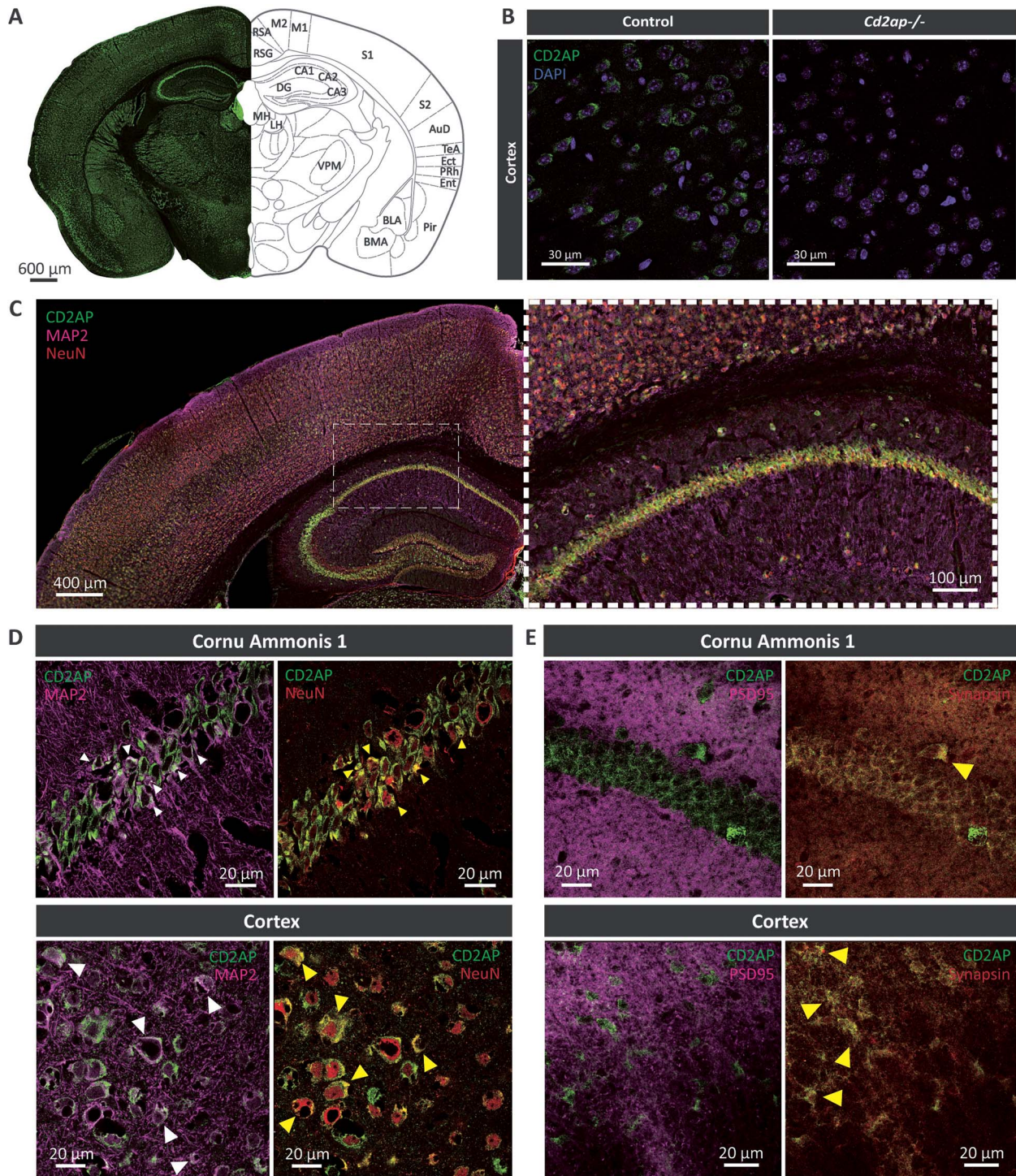


Figure 1. *Cd2ap* is neuronally expressed and localizes to synapses in hippocampus and cortex. (A) *Cd2ap* is expressed ubiquitously in the adult mouse brain (coronal slice at bregma ~ -1.58 mm), including in the hippocampus cornu ammonis (CA) and dentate gyrus (DG) and in cortex. Other areas of *Cd2ap* expression include thalamus [ventral posteromedial nucleus (VPM) labeled], habenula [medial (MH) and lateral (LH) habenula indicated], and amygdala [basolateral amygdala (BLA) and basomedial amygdala (BMA) indicated]. Other abbreviations: RSA=retrosplenial agranular cortex, RSG=retrosplenial granular cortex, M1=primary motor cortex, M2=supplementary motor cortex, S1=primary somatosensory cortex, S2=second somatosensory cortex, AuD=auditory cortex, TeA=temporal cortex, Ect=ectorhinal cortex, PRh=perirhinal cortex, Ent=entorhinal cortical area, Pir=piriform cortex. (B) CD2AP cortical staining with the anti-CD2AP antibody (green) in wildtype controls is mostly abolished in animal homozygous for the germline knockout allele (*Cd2ap*^{-/-}). Nuclei are counterstained with DAPI (blue). Representative images from 5-week-old mouse brain slices stained. See also Fig. S1A. (C) *Cd2ap* is expressed in neurons. Mouse brain slices were co-stained for CD2AP (green) and neuronal markers, including MAP2 (neuronal perikarya and dendrites; magenta) and NeuN (neuronal nuclei; red). Hippocampal CA1 region (indicated by dashed rectangle) shown at higher power (right). See Fig. S2A for additional images and Fig. S3A for complementary studies of cultured neurons. (D) CD2AP (green) shows overlapping localization with the neuronal markers MAP2 (magenta) and NeuN (red) in the hippocampus CA1 region and the cortex. Colocalization indicated by white or yellow, for CD2AP staining overlapping with MAP2 or NeuN, respectively (arrowheads). (E) CD2AP shows overlapping localization with the pre-synaptic marker, Synapsin (red) but not the post-synaptic marker, PSD95 (magenta) in the CA1 and the cortex. Colocalization of CD2AP with Synapsin is indicated by yellow (arrowheads). See also Fig. S2B for additional images and Fig. S3B for complementary studies of cultured neurons.

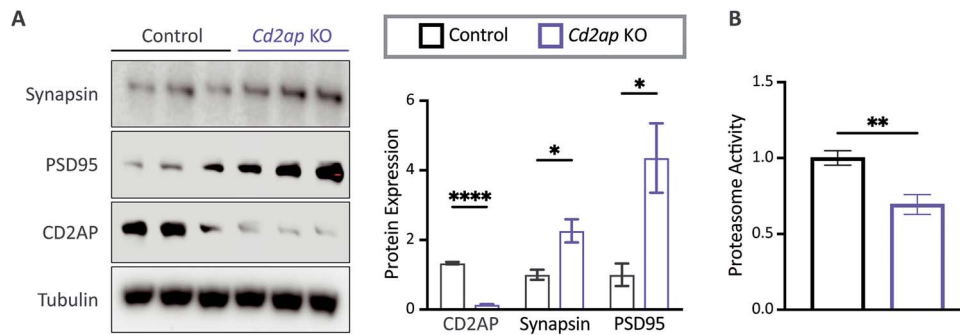


Figure 2. Loss of *Cd2ap* disrupts neuronal proteostasis. (A) CRISPR-mediated knockout (KO) of *Cd2ap* in mouse primary Cas9 neurons results in increased expression of Synapsin and PSD95, and decreased expression of CD2AP compared to control neurons transfected with AAV expressing guide sequences targeting *LacZ*. Statistical analysis was based on t-tests with sample sizes $N=3$ per genotype. Western blots were performed on homogenates from DIV21 neurons. Protein expression was normalized against tubulin expression. * $P < 0.05$; **** $P < 0.0001$. All error bars denote mean \pm SEM. (B) *Cd2ap* KO primary neurons show decreased activity of the ubiquitin proteasome system. Statistical analysis based on t-test with sample size $N = 10$ per genotype. Proteasome activity assay was completed on homogenates from DIV21 neurons. ** $P < 0.01$. Error bar denotes mean \pm SEM.

Cd2ap^{-/-} mice showed increased apical dendritic spine density, whereas spine density was decreased on basal dendrites. Interestingly, heterozygous *Cd2ap*^{+/-} mice also displayed a decrease in spine density on basal dendrites (Fig. 3D). Overall, our results further reinforce a conserved neuronal role for *Cd2ap* in synapse maturation and proteostasis in the mammalian central nervous system.

***Cd2ap* shows haploinsufficient requirements for short-term synaptic plasticity**

We next performed *ex vivo* electrophysiology to examine the functional consequences of *Cd2ap* loss on synaptic connectivity and plasticity. For this, we first recorded pyramidal neurons from the hippocampal CA1 region (Fig. 4A), given its vulnerability in early AD [1, 39] as well as the strong *Cd2ap* expression detected in this region (Fig. 1 and Fig. S2). We initially confirmed that basal neuronal membrane properties were unaffected following *Cd2ap* loss-of-function, based on recordings from acute brain slices from 5 to 8-week old mice that were either homozygous or heterozygous for the *Cd2ap* germline knockout allele (Fig. S7). We also documented no significant changes in spontaneous miniature excitatory post-synaptic current (mEPSC) frequencies (Fig. 4B). To further interrogate the hippocampal circuit, we next performed extracellular recordings of evoked field excitatory post-synaptic potentials (fEPSPs) in CA1 while stimulating Schaffer collaterals to determine whether loss of *Cd2ap* impacts paired-pulse facilitation, an established test of pre-synaptic plasticity [40]. In this experiment, two pre-synaptic stimuli are delivered in close succession, and facilitation is calculated as the ratio of the second post-synaptic response to the first response. We discovered a significant increase in hippocampal paired-pulse facilitation in *Cd2ap*^{-/-} mice (Fig. 4C and D), consistent with a decreased probability of vesicle release and altered pre-synaptic plasticity [40]. As introduced above, prior work established haploinsufficient requirements for *Cd2ap* in maintaining glomerular integrity within the kidney [13]. Interestingly, we found that heterozygous *Cd2ap*^{+/-} mice also manifest elevated paired-pulse facilitation (Fig. 4C-E), consistent with a haploinsufficient requirement for hippocampal plasticity.

***Cd2ap* is largely dispensable for learning and memory in young and aged mice**

Germline knockout of *Cd2ap* causes progressive kidney failure and death by approximately 7 weeks [16], precluding a comprehensive

survey of potential nervous system function in aged animals. We therefore generated a new mouse model harboring a floxed allele (*Cd2ap*^{fl/fl}), enabling nervous system-specific knockout of *Cd2ap* when crossed with a *Nestin-Cre* driver (*Nes-Cre*) [41]. We confirmed that *Cd2ap*^{fl/fl};*Nes-Cre* animals showed significantly reduced expression of *Cd2ap* (Fig. S8) and survived past 7 weeks-of-age. We next performed a battery of behavioral tests in 3.5- and 12-month-old conditional knockouts, circumventing any potential confounding effects due to its essential role in the kidney. Our comprehensive behavioral analyses included tests of locomotor activity (open field assay), anxiety (elevated plus maze and open field assay), pain response (hot plate test), and memory (novel object recognition and Y-maze test). Unexpectedly, *Cd2ap*^{fl/fl};*Nes-Cre* conditional knockout mice showed little to no significant differences in behavior compared to *Cd2ap*^{fl/fl} control mice, in either young or aged animals (Figs 5 and S9). Among otherwise negative behavioral findings, the only outlier differences we observed included transient changes in locomotor activity in *Cd2ap* conditional knockout mice during the first and last 10 min of the open field assay, but these differences were not consistent between young and aged animals (Fig. 5). In addition, 3.5-month-old *Cd2ap* animals showed significant differences during training in fear conditioning assays, but performed similar to wildtype controls during the actual test (Fig. S9A).

Given our findings from hippocampal neurophysiology above, we also considered the possibility of haploinsufficient requirements for *Cd2ap* in memory and other behaviors. Mice heterozygous for a germline null allele (*Cd2ap*^{+/-}) have previously been evaluated by the International Mouse Phenotyping Consortium [42, 43]. Specifically, *Cd2ap*^{+/-} mice showed no significant differences in performance when compared to wildtype mice when examined at 8–9 weeks of age, including the open field assay, light–dark test, pre-pulse inhibition, or grip strength. We therefore deployed a more sensitive, automated touch screen behavioral assay [43–45] with prior validity in published studies of AD and other neuropsychiatric disease models [43, 46, 47]. In this cognitive test, mice learn to select the correct shape from a pair of visual stimuli (Fig. 6A) [43–45]. These time-intensive assays, requiring more than 12 months for testing of the full cohort, were initiated with *Cd2ap*^{+/-} mice prior to the availability of *Cd2ap*^{fl/fl} conditional knockout models. Wildtype and *Cd2ap*^{+/-} heterozygous mice, each aged to 2.5 months, were required to successfully complete both positive and negative reinforcement training prior to the pairwise visual discrimination test (Fig. 6B).

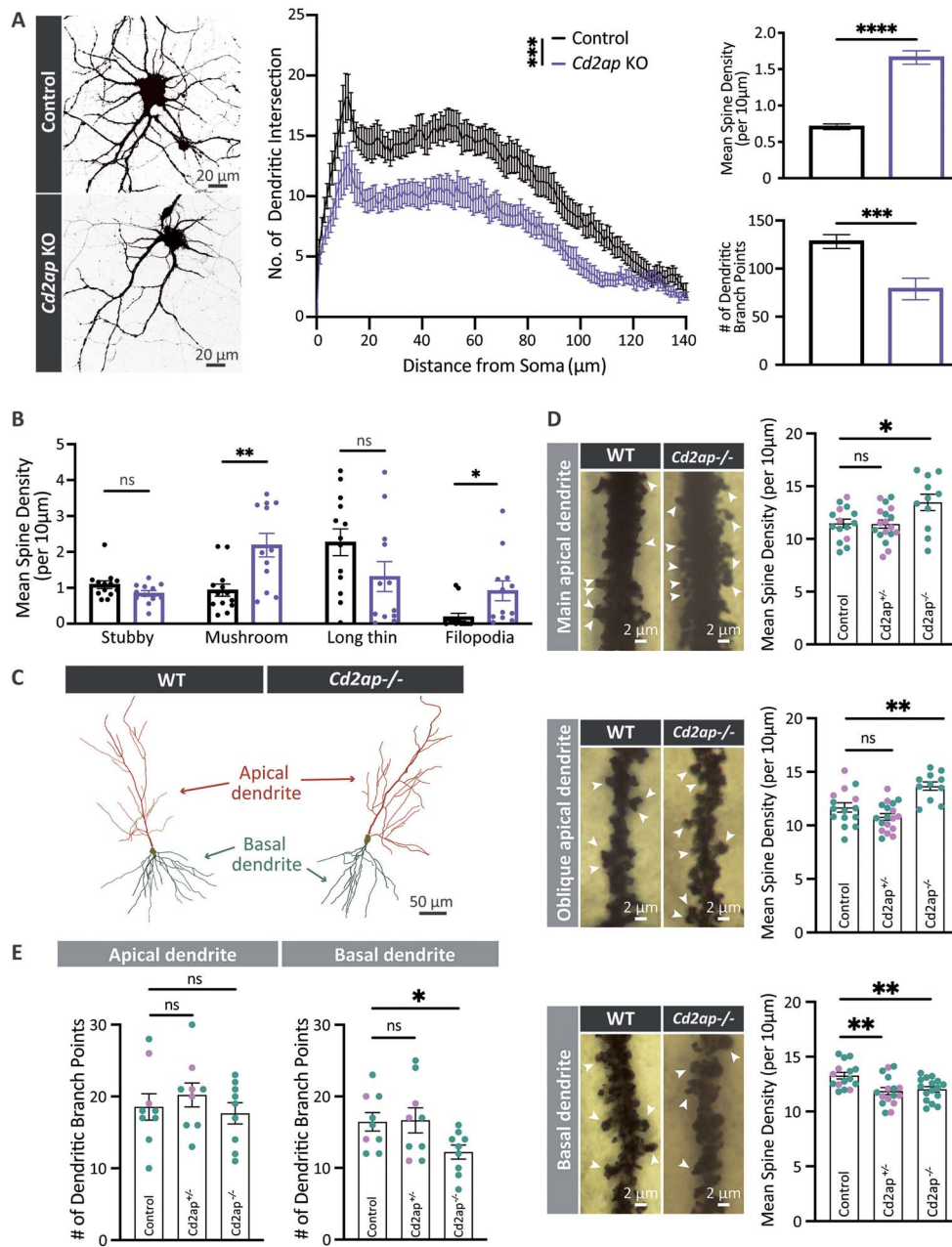


Figure 3. Loss of *Cd2ap* disrupts neuronal and synaptic morphology. (A) CRISPR-mediated knockout (KO) of *Cd2ap* in mouse primary Cas9 neurons results in increased dendritic spine density and fewer dendritic branch points at DIV21. Control Cas9 neurons were transfected with control AAV expressing guide sequences targeting *LacZ*. Statistical analysis of dendritic spines and branchpoints was based on t-tests, with sample size (N) = 20 and 19 cells for *Cd2ap* controls, respectively. *Cd2ap* KO primary neurons also show a decrease in the number of dendritic intersections based on Sholl analysis, based on statistical analysis using linear mixed-effects models with N = 18 or 15 cells for *Cd2ap* and controls, respectively. ns, non-significant; *** $P < 0.001$; **** $P < 0.0001$. All error bars denote mean \pm SEM. (B) *Cd2ap* KO neurons show increased density of mushroom spines and filopodia, but unchanged stubby or long thin spines, based on t-tests. Density calculated as number of spines per $10\mu\text{m}$ of dendrite. N = 12 and 13 cells for *Cd2ap* or control, respectively. ns, non-significant; * $P < 0.05$; ** $P < 0.01$. All error bars denote mean \pm SEM. (C) Representative CA1 hippocampal pyramidal neuron traces showing the analyzed apical and basal dendritic trees of 5–6-week-old wildtype control (WT) and *Cd2ap*^{-/-} mice. (D) *Cd2ap*^{-/-} mice have increased spine density on both main and oblique apical dendrites. Arrowheads indicate representative spines. By contrast, basal dendrites show decreased spine density in both *Cd2ap*^{-/-} and *Cd2ap*^{+/-} mice. Statistical analysis was based on t-tests. For apical dendrites, samples sizes (number cells quantified) were WT = 15 (4F and 11M); *Cd2ap*^{+/-} = 18 (10F and 8M); and *Cd2ap*^{-/-} = 11 (11M). For basal dendrites samples sizes were WT = 15 (4F and 11M); *Cd2ap*^{+/-} = 16 (8F and 8M); and *Cd2ap*^{-/-} = 16 (16M). Cells were counted from at least 2 independent animals per genotype. ns, non-significant; * $P < 0.05$; ** $P < 0.01$. All error bars denote mean \pm SEM. See also Fig. S6 for results of Sholl analyses. (E) Dendritic branching of basal but not apical dendrites is decreased in *Cd2ap*^{-/-} mice. No change was observed in *Cd2ap*^{+/-} heterozygotes for either apical or basal dendrites. Statistical analysis was based on t-tests, with N = 9 cells for each group. Sex distribution of the cells' animals of origin was as follows: WT had 2F and 7M cells; *Cd2ap*^{+/-} had 3F and 6M cells; and *Cd2ap*^{-/-} had all M cells. ns, non-significant; * $P < 0.05$. All error bars denote mean \pm SEM. The color of individual data points in panel (D) and (E) bar graphs indicates the sex of the animal of origin for each cell, with teal indicating male mice and lavender indicating female mice. Samples sizes (number of mice) used for analyses in (D) and (E) were WT = 4 (1F and 3M); *Cd2ap*^{+/-} = 4 (2F and 2M); and *Cd2ap*^{-/-} = 2 (2M). Given the unequal distribution of males and females in the control versus *Cd2ap*^{-/-} groups in (D) and (E) we cannot exclude sex effects as a potential source of variability. See also Fig. S13 panels A-B for the animal of origin distribution for all cells analyzed in D and E and a display of potential effects of animal-dependent variability.

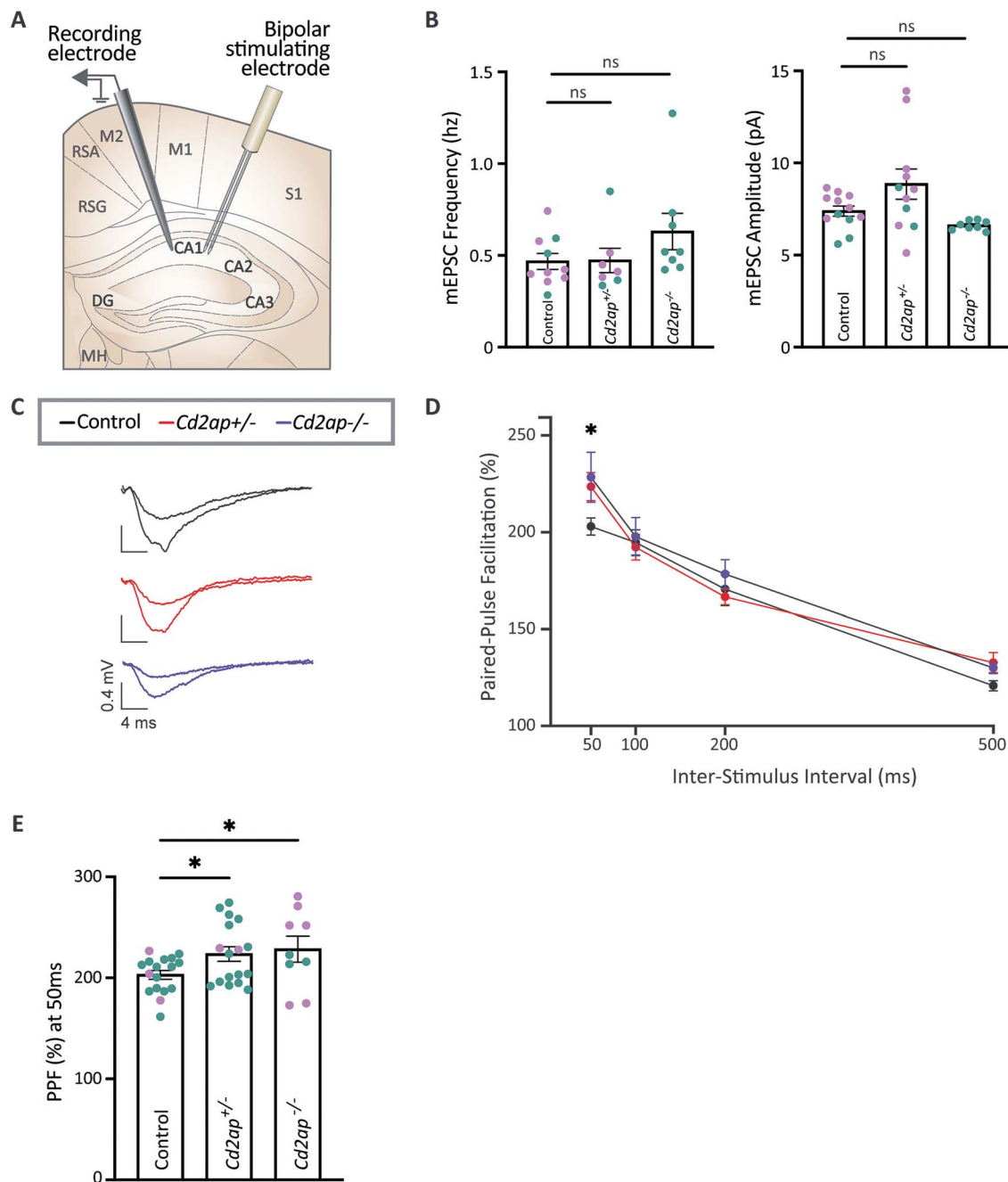


Figure 4. *Cd2ap* is required for short-term hippocampal plasticity. (A) Graphical representation of the setup for recording from Schaffer collaterals of the hippocampal CA1 region. (B) mEPSC frequency and amplitude are not significantly changed in *Cd2ap* homozygous or heterozygous animals ($P > 0.05$; ns, non-significant), when compared with wildtype controls (WT). All electrophysiological recordings were performed in acute coronal brain slices from 5 to 8-week old animals (mean 6.7 weeks). Statistical analysis was performed using one-way ANOVA with Dunnett's post-hoc test. For analysis of mEPSC frequency, sample sizes (N cells recorded) were as follows: WT = 10 (7 female and 3 male); *Cd2ap*^{+/-} = 7 (4F and 3M); and *Cd2ap*^{-/-} = 8 (8M). For analysis of mEPSC amplitude, sample sizes were as follows: WT = 12 (8F and 4M); *Cd2ap*^{+/-} = 11 (8F and 3M); and *Cd2ap*^{-/-} = 8 (8M). Samples sizes (number of mice) were WT = 7 (4F and 3M); *Cd2ap*^{+/-} = 5 (3F and 2M); and *Cd2ap*^{-/-} = 4 (4M). All error bars denote mean \pm SEM. See also Fig. S7 for additional neurophysiology examining basal membrane properties. (C) Representative traces from paired pulse facilitation (PPF) trials, recorded from the hippocampal CA1 Schaffer collaterals in WT, *Cd2ap*^{+/-}, and *Cd2ap*^{-/-} animals. The top trace recorded from each genotype is the excitatory post-synaptic potential (EPSP) response to the first PPF pulse, and the bottom, larger trace is the EPSP response to the second pulse. To obtain PPF, the slope (mV/ms) of the rising phase at the initial segment of each response is measured and PPF is calculated as the ratio of EPSP slopes (second pulse/first pulse). (D) PPF is increased in both *Cd2ap* homozygous and heterozygous animals, when compared with WT controls for the 50 ms inter-stimulus interval (ISI) trial. Statistical analysis was performed using two-way ANOVA with Holm-Šidák's post-hoc test, with sample sizes (slices recorded): WT = 17 (3F and 14M); *Cd2ap*^{+/-} = 17 (2F and 15M); and *Cd2ap*^{-/-} = 9 (6F and 3M). Samples sizes (number of mice) were WT = 10 (1F and 9M); *Cd2ap*^{+/-} = 9 (1F and 8M); and *Cd2ap*^{-/-} = 5 (2F and 3M). * $P < 0.05$. All error bars denote mean \pm SEM. (E) Bar graph shows increase in PPF in *Cd2ap* homozygous and heterozygous animals at 50 ms ISI. Teal data points are from recording on slices from male mice and lavender data points are from recording on slices from female mice. * $P < 0.05$. All error bars denote mean \pm SEM. The color of individual data points in panel (B) and (E) bar graphs indicates the sex of the animal of origin for each cell, with teal indicating male mice and lavender indicating female mice. Given the unequal distribution of males and females in the control versus *Cd2ap*^{-/-} groups in (B) and (E) we cannot exclude sex effects as a potential source of variability. See also Fig. S13 panels C-D for the animal of origin distribution for all cells/slices analyzed in (B) and (E) and a display of potential effects of animal-dependent variability.

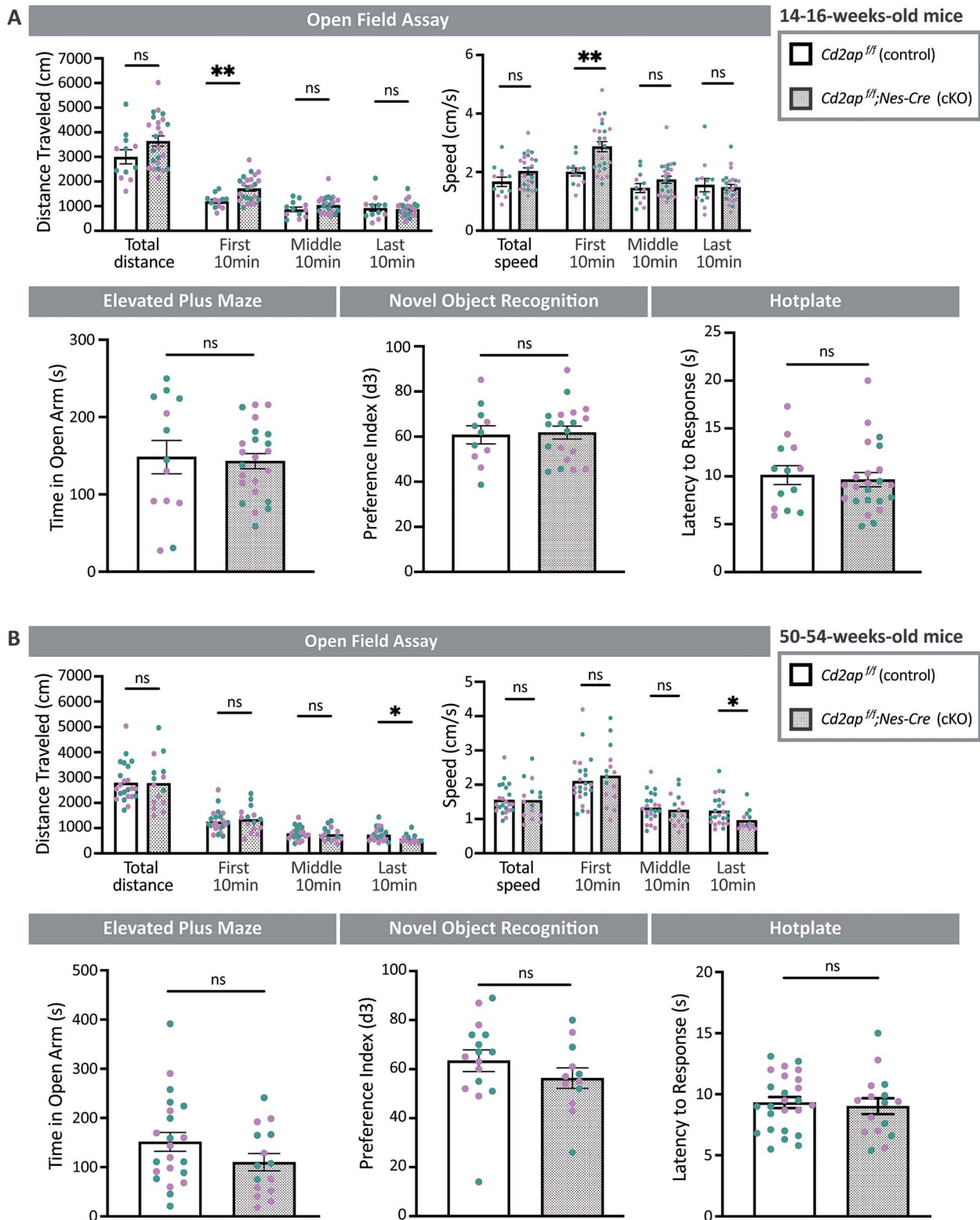


Figure 5. *Cd2ap* is largely dispensable for cognitive and motor behaviors. Representative results are shown from behavioral assessments of *Cd2ap* conditional knockout animals (cKO; *Cd2ap^{fl/fl};Nes-Cre*) and controls (*CD2AP^{fl/fl}*). Mice were examined at either 3.5 (A) or 12 months of age (B). Overall, no significant differences were detected (all $P > 0.05$), except for increased locomotor activity for 12-month-old *Cd2ap* cKO during the last 10 min of the open field assay. Statistical analysis was based on t-tests. For assessments of young mice, samples sizes of $N = 23$ cKO (13F and 10M) and 13 control (6F and 7M) mice were used for the elevated plus maze and hot plate tests; $N = 24$ cKO (14F and 10M) and 12 control (5F and 7M) mice for open field; and $N = 19$ cKO (with 10F and 9M) and 11 (with 5F and 6M) control mice were examined for novel object preference. For studies of aged mice, sample sizes were of $N = 15$ cKO (9F and 6M) and 22 control (10F and 12M) mice were used for the elevated plus maze tests; $N = 15$ cKO (with 9F and 6M) and 23 control (11F and 12M) mice for open field; $N = 12$ cKO (7F and 5M) and 16 control (7F and 9M) mice for novel object preference; and $N = 16$ cKO (9F and 7M) and 25 controls (10F and 15M) for hotplate testing. The color of individual data points indicates the sex of each animal, with teal indicating male mice and lavender indicating female mice. ns, non-significant; * $P < 0.05$; ** $P < 0.01$. All error bars indicate mean \pm SEM. See also Fig. S9 for results of additional assays.

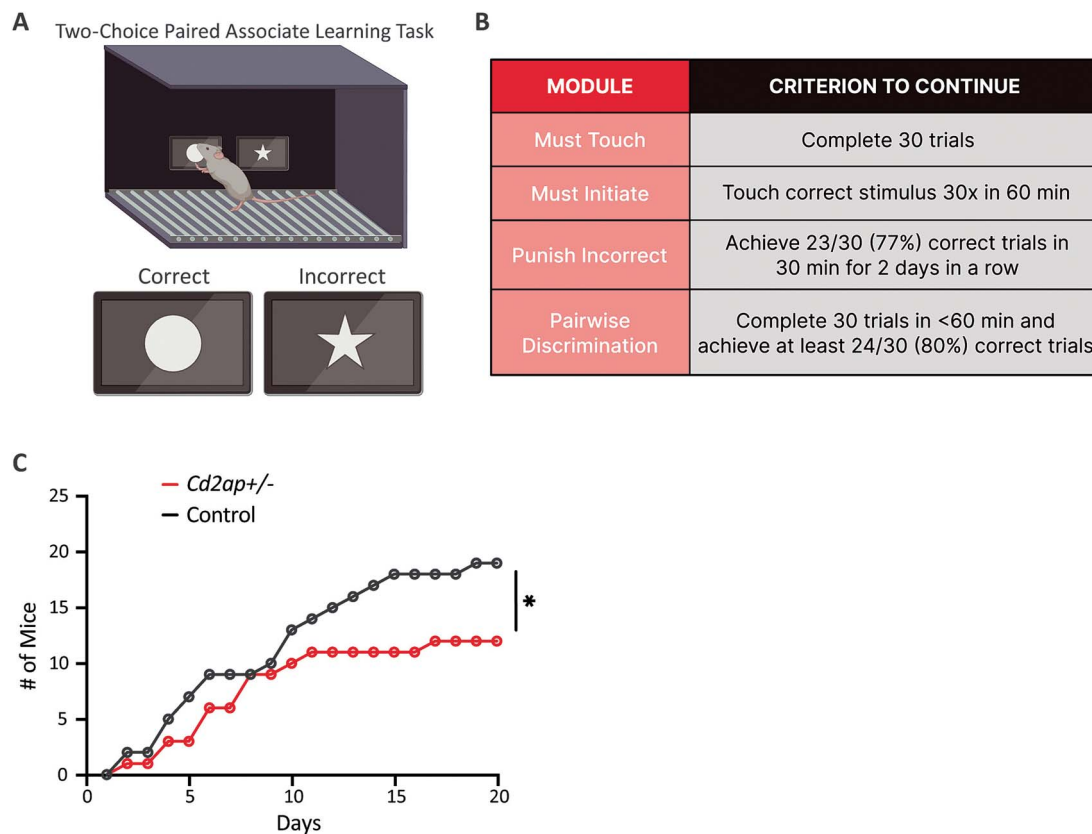


Figure 6. Haploinsufficient requirement of *Cd2ap* for pairwise visual discrimination. (A) Schematic of the behavioral chamber set-up, including an illustration of the stimuli displayed on the touchscreen. (B) Experimental design and criteria for progressing through each training module, including “must touch,” “must initiate,” and “punish incorrect”, prior to pairwise discrimination testing. (C) *Cd2ap*^{+/-} heterozygous mice (N=18, 9F and 9M) showed impaired discrimination learning compared with wildtype controls (N=21, 10F and 11M) when tested at 2.5 months of age, with fewer animals successfully reaching the pre-specified criteria for success by day 20, based on statistical analysis using the t-test. *P < 0.05. Among those animals that successfully pass the test, there was no significant difference in the time required to achieve success (see Fig. S10C). See also Fig. S10D for a breakdown of the N of mice that satisfied criteria for each module of the assay.

Notably, *Cd2ap*^{+/-} animals showed significantly delayed learning during the initial training phase, in which they were required to touch the screen to receive a reward (Fig. S10A). Subsequently, during the final testing phase, *Cd2ap*^{+/-} mice showed impaired discrimination learning compared with wildtype controls, with fewer animals successfully reaching the pre-specified criteria for success (Fig. 6C). Since the *Cd2ap*^{+/-} mice tested in this experiment, heterozygous for the germline loss-of-function allele, are expected to have haploinsufficiency across all tissues and cell types, it is possible that observed behavioral impairment arises from a requirement in either neurons, other brain cells (e.g. microglial or endothelial cells), or possibly even other tissues. Nevertheless, these results were overall consistent with a subtle, haploinsufficient requirement for *Cd2ap* in pairwise discrimination, but *Cd2ap* appeared otherwise dispensable for general nervous system function, based on our broad survey of cognitive and motor behavioral phenotypes.

***Cd2ap* triggers dose-sensitive protein signatures of altered proteostasis and synaptic dysfunction**

To further explore the molecular consequences of *Cd2ap* loss, we performed mass-spectrometry proteomics on hippocampi from approximately 5-week-old mice, examining *Cd2ap*^{-/-} homozygotes versus wildtype controls. Our quality-controlled dataset included 8478 proteins for analyses. We detected 832 significantly differentially expressed proteins in hippocampal tissue lacking

Cd2ap when compared with wildtype brain tissue, including 602 up-regulated and 230 down-regulated proteins (Fig. 7A and B and Table S1). As expected from our phenotypic characterization, loss of *Cd2ap* induced differential expression of proteins with roles in proteostasis and synaptic transmission, based on gene ontology term enrichment analysis (Fig. 7C, Fig. S11, Tables S2 and S3). Specifically, our analysis identified perturbations among proteasome subunits (PSMD4 and UCHL5), components of the ubiquitin machinery (multiple ring finger domain-containing proteins), as well as chaperones, including DNAJA1. We also discovered numerous regulators of synaptic structure and function, including GABRA1, DLGAP4, and BDNF. Interestingly, *Cd2ap* KO was also unexpectedly associated with perturbations in lipid metabolism, including up-regulation of several apolipoproteins (e.g. APOA1, APOC1, and APOC3).

Given our findings of potential haploinsufficient requirements for *Cd2ap* in synaptic structure/function and visual pairwise discrimination, hippocampi from *Cd2ap* heterozygotes were additionally included for generation of proteomic profiles (e.g. together with controls and *Cd2ap* homozygotes in the same batch). We discovered 508 significantly differentially expressed proteins in hippocampal tissue from *Cd2ap*^{+/-} hippocampi, consisting of 323 up- and 185 down-regulated proteins (Fig. 7A, Fig. S11A and B, and Table S1). Importantly, our analyses revealed enrichment for many overlapping biological pathways (Figs 7C and S11B–D; Tables S2 and S3). Indeed, 26% (133 out of 508) of differentially

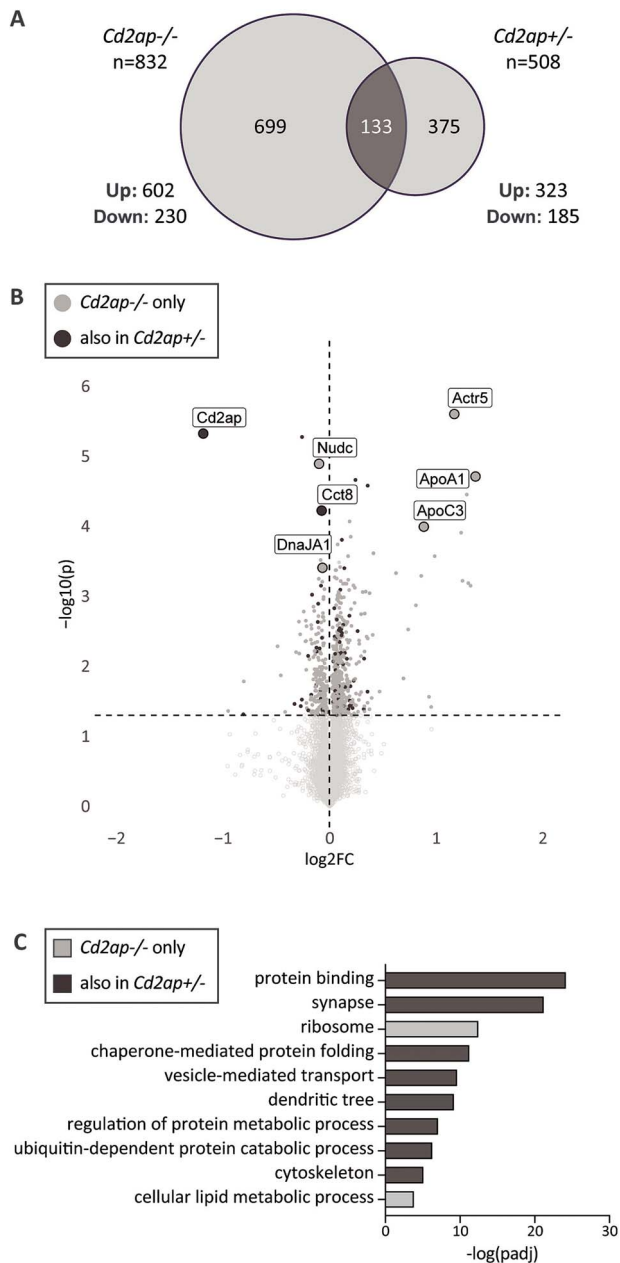


Figure 7. *Cd2ap* loss triggers protein signatures of altered proteostasis, lipid dysmetabolism, and synaptic dysfunction. (A) At 5-weeks of age, *Cd2ap* homozygous and heterozygous animals have significantly overlapping hippocampal differential expression signatures, when compared with wildtype controls. Differentially expressed proteins were $P < 0.05$, and overlap for directionally concordant changes was based on Fisher's exact test ($P = 1.58 \times 10^{-26}$). 130 out of 133 overlapping, differentially expressed proteins were concordant. One dissected hippocampus from 5 animals per genotype were profiled ($N = 5$ each for wildtype, *Cd2ap*^{-/-}, and *Cd2ap*^{+/-}; with 2 female and 3 male wildtype, 3F and 2M *Cd2ap*^{-/-}; and 3F and 2M *Cd2ap*^{+/-}). See also Fig. S11 and Table S1 for full results. (B) Volcano plot highlighting results from differential expression analysis of *Cd2ap*^{-/-} homozygous animals vs. wildtype controls. Significantly differentially expressed protein ($P < 0.05$, dotted horizontal line) are indicated with dark gray). Proteins highlighted in black were consistently differentially expressed in *Cd2ap*^{+/-} heterozygotes. The residual *Cd2ap* protein signal in the *Cd2ap*^{-/-} germline null animal is likely attributable to background chemical noise, possibly stemming from tandem mass tag isotope impurity. See also Fig. S11 and Table S1. (C) Gene ontology term enrichment analysis highlights significant pathways affected in *Cd2ap*^{-/-} animals (Fisher's exact test false discovery rate $P < 0.05$). Representative terms were selected from among the top results. Darker bars denote pathways that are consistent affected in *Cd2ap*^{+/-} heterozygous animals. See also Fig. S11 and Table S2 for full results.

expressed proteins from *Cd2ap*^{+/-} heterozygotes were also seen in *Cd2ap*^{-/-} homozygotes, comprising a highly significant overlap ($P = 1.6 \times 10^{-26}$) (Fig. 7A). Further, 130 out of 133 (97.7%) of these overlapping differentially expressed genes were in fact concordant. In fact, out of 1207 unique differentially expressed proteins from either comparison, there was an 82.3% concordance in direction of expression (Fig. S12). Thus, partial loss of *Cd2ap* causes a proteomic signature similar to complete loss-of-function, consistent with a dose-sensitive, haploinsufficient requirement.

Discussion

CD2AP is an AD susceptibility gene candidate, but its potential role in the adult nervous system has remained undefined, impeding a comprehensive understanding of its contribution in disease. Here, we show that CD2AP protein is broadly expressed in the mammalian brain, including in hippocampus, and is present at the synapse. Following conditional nervous system knockout and a comprehensive behavioral analysis, *Cd2ap* was largely dispensable for cognitive and motor behaviors. Nevertheless, findings from both *in vitro* and *in vivo* studies, along with proteomics, converge to implicate *Cd2ap* with a regulatory role in synaptic proteostasis and plasticity, and we speculate that its activity could become critical during stress conditions. Lastly, our results highlight dose-sensitive, haploinsufficient requirements in the nervous system, suggesting how modest perturbations in CD2AP expression might impact AD risk and pathogenesis.

Tissue and cell type-specific expression patterns can help pinpoint the causal genes responsible for susceptibility signals from GWAS, and further provide important clues to potential mechanisms in disease. In particular, eQTL analysis can link specific risk variants to altered expression. Consistent with prior work [17, 19, 27, 48], we document *Cd2ap* expression throughout the mouse brain, and within multiple cell types. Importantly, we also show that AD-associated risk variants at the CD2AP locus selectively increase gene expression in microglia and neurons. While substantial recent work has focused on how AD susceptibility genes function in microglia to alter immune-mediated mechanisms, less is known about potential roles within neurons and at the synapse. Nevertheless, synaptic loss is strongly associated with the earliest clinical manifestations of AD [49–51]. Several key findings from this work support a requirement for CD2AP at the mammalian synapse. First, using a new antibody, we highlight robust and specific CD2AP expression within mouse hippocampal and cortical neurons, and further demonstrate protein localization at the pre-synapse. Second, based on the paired pulse facilitation assay, germline knockout of *Cd2ap* disrupts synaptic plasticity, which is largely dependent on pre-synaptic mechanisms [40]. Third, deletion of *Cd2ap* from primary cultured neurons caused reduced dendritic branching and increased synaptic spines, and we observed related changes in the hippocampus of *Cd2ap*^{-/-} mice. Finally, proteomic profiles from *Cd2ap* knockout mice revealed signatures of altered synaptic processes.

While the precise mechanism(s) for CD2AP at the synapse remain to be determined, our results along with prior published findings provide several important clues. In our recordings from hippocampus, spontaneous synaptic vesicle release (mEPSCs) was normal in the absence of *Cd2ap*, whereas paired pulse facilitation was abnormally increased. This suggests that *Cd2ap* is dispensable for processes governed by resting Ca^{2+} , but may be important for activity dependent synaptic processes that rely on Ca^{2+} kinetics. Specifically, increased facilitation following loss of

Cd2ap is consistent with an overall reduced probability of synaptic vesicle release, leading to a larger pool of vesicles triggered during the subsequent pulse [40]. We previously showed that loss of the *Drosophila* CD2AP homolog, *cindr*, caused reduced pre-synaptic Ca^{2+} , and similarly enhanced facilitation during rapid stimulation at the neuromuscular junction [9]. It is possible that CD2AP either directly participates in synaptic vesicle priming and release, consistent with its established role in endocytosis and vesicle trafficking [20, 26, 52], or alternatively, it could more indirectly regulate neuronal Ca^{2+} homeostasis. In both the *Drosophila* and mouse brain, loss of *Cd2ap/cindr* triggers elevated levels of the major Ca^{2+} efflux transporter, PMCA, possibly due to altered ubiquitin-proteasome activity [9]. Indeed, the proteasome is important for maintenance of many synaptic functions, and dysregulated turnover of PMCA, Synapsin, and other key proteins may explain the altered short-term plasticity following loss of *Cd2ap* [53, 54]. In the future, it may be interesting to examine whether long-term potentiation and/or depression also require *Cd2ap*, as the proteasome has also been implicated in these synaptic plasticity phenomena [55]. Besides its contribution to neuronal physiology, *Cd2ap* also appears to have an evolutionary conserved role in synapse formation or maturation. At the *Drosophila* neuromuscular junction, *cindr* mutants show aberrant, incompletely differentiated synaptic boutons [9]. We also discovered an increase in synaptic spines within primary mouse neuronal cultures, including the observation of immature filopodia morphology; and *in vivo*, we documented an analogous increase in spine density at apical dendrites of hippocampal pyramidal neurons. It is possible that opposing and proportional shifts in synaptic spine numbers along apical or basal dendrites, perhaps with concomitant changes in dendritic branching, may explain why mEPSC frequency is unaffected following *Cd2ap* loss. Altered synapse numbers may also represent a compensatory response to impaired synaptic vesicle release or other related circuit dysfunction. Alternatively, CD2AP may have separable roles in both synapse development and function. For example, CD2AP has been shown to regulate actin cytoskeleton dynamics [20, 56], which in turn, is an important contributor to synaptic spine morphology, axonal outgrowth, and dendritic arborization [57]. Following *Cd2ap* knockout, we found that primary cortical neuron cultures showed decreased dendritic branching. Potentially consistent with our findings, a previous study demonstrated that *Cd2ap* overexpression reciprocally leads to increased neurite branch complexity in rat neuronal cultures [17].

Given its brain expression and requirement for synaptic structure and function, it is perhaps unexpected that *Cd2ap* was largely dispensable for locomotor and cognitive behaviors, based on our comprehensive survey. Since *Cd2ap* germline knockout causes progressive kidney failure and animals die by 7 weeks, we developed and characterized a conditional knockout allele, in which *Cd2ap* was removed specifically from the adult nervous system. Our findings of normal behavior in 12-month-old animals were consistent with results from prior studies of mice homozygous for the germline *Cd2ap* knockout allele, but including a nephrin promoter-driven transgenic construct that restores *Cd2ap* expression in the kidney [19]. Thus, despite the important role of synaptic plasticity for memory encoding in the hippocampus, our results do not support a major requirement for *Cd2ap* in this process. However, there are a few notable caveats. First, as alluded to above, we cannot exclude the possibility of adaptive synaptic or circuit mechanisms that may compensate for potential *Cd2ap* behavioral requirements. Second, it is also plausible that the brain-expressed CD2AP

paralog, CIN85 (69% similarity/37% identity), may functionally substitute [58–62]. Lastly, we note that our studies of synapse neurophysiology and morphology were performed using the germline knockout (*Cd2ap^{-/-}*); whereas our behavioral survey used the conditional knockout (*Cd2ap^{f/f};Nes-Cre*), somewhat limiting inter-comparability. Although our experiments were conducted prior to fulminant decompensation of renal function in *Cd2ap^{-/-}* mice, we cannot definitively exclude that early metabolic changes may have also contributed. However, we note that similar synaptic morphological changes were observed in primary neuronal cultures, following CRISPR-mediated deletion. It is also possible that the complete germline knockout removes *Cd2ap* function among additional brain cell types, such as microglia and endothelial cells, that are poorly targeted by *Nestin-Cre* [63], which expresses primarily in neuronal and astrocytic precursors. For example, based on prior published work, *Cd2ap* may be required in endothelial cells to maintain the blood–brain barrier [19].

Our findings add to prior work suggesting conserved dose-sensitive, haploinsufficient requirements for *Cd2ap*. Inherited loss-of-function mutations in CD2AP cause autosomal dominant kidney disease, and age-dependent, progressive renal dysfunction has been recapitulated in heterozygous *Cd2ap^{+/-}* mice [13–16]. Here, we show that *Cd2ap^{+/-}* mice manifest enhanced paired pulse facilitation similar to homozygous littermates, and we further found evidence for decreased synaptic spine density in heterozygotes. We also discovered a possible haploinsufficient requirement for visual discrimination learning, which is dependent on the hippocampus [64]. Perhaps most striking, *Cd2ap* heterozygous mice revealed hippocampal differential protein expression signatures that significantly overlapped with that seen in complete knockout animals, including similar enrichment for synaptic proteins and ubiquitin-proteasome system components. We note, however, that our proteomic results do not support an additive, dose-response for *Cd2ap* loss on differential expression fold-change for most proteins (Fig. S11A). Nevertheless, dose-sensitive requirements may be an important hallmark for genes like CD2AP that are implicated in AD risk, since most GWAS susceptibility signals represent the impact of common regulatory variants causing modest changes in gene expression.

Notably, our evaluation of *Cd2ap* function in the mouse brain reveals links to several processes strongly connected to AD pathogenesis [65–68]. For example, the ubiquitin-proteasome system, synaptic morphology/plasticity, and discrimination learning are all compromised in AD mouse models [69–74], and our findings implicate *Cd2ap* in each of these contexts. Recent work supports early impairments in brain proteostasis in AD pathogenesis [75, 76] and pharmacologic activation of the proteasome was protective in both AD cell culture and animal models [75, 77]. The ubiquitin-proteasome system is also required for normal synaptic structure and function, including in the hippocampus, with CD2AP potentially playing a dual role in the context of both healthy aging and disease [9, 76]. Based on proteomics, we also unexpectedly discovered that *Cd2ap* loss-of-function triggered increased expression of multiple apolipoproteins, including ApoC1 and ApoC3, both of which are known to interact with Apolipoprotein E (ApoE) [78, 79]. In humans, the APOE epsilon-4 allele is among the most common and potent genetic risk factors for AD [80]. Several other genes with roles in lipid metabolism have also been implicated by AD GWAS, including SORL1, CLU, and ABCA7 [12, 81, 82].

Based on single cell eQTL analysis, the AD risk variant at the CD2AP locus causes a modest but significant increase in

CD2AP mRNA levels, including within neurons and microglia. Since our studies focus exclusively on the characterization of CD2AP loss-of-function, it would be interesting in future work to additionally consider the consequences of modest CD2AP over-expression. Complementary genetic manipulations of CD2AP in microglia would also be valuable given the growing evidence supporting an important role for other microglial genes (e.g. TREM2, SPI1, CD33) and immune-mediated mechanisms in AD risk [83–88]. While CD2AP was initially discovered for its participation in immune signaling [11], to our knowledge, there have not yet been any studies in microglia. Lastly, it will also be important to determine whether *Cd2ap* gain- or loss-of-function impacts other established AD mechanisms, including amyloid-beta- or tau-mediated neurodegeneration. In *Drosophila*, CD2AP loss-of-function enhanced tau-mediated neurodegeneration, possibly via convergent impact on the ubiquitin-proteasome system [9, 25]. In cell culture, CD2AP knockdown altered endocytic trafficking of the Amyloid- β precursor protein (APP), enhancing amyloidogenic processing [26]. Neither of these results support a simple model in which reduced expression of CD2AP may lower AD risk, as suggested by our eQTL analysis. Conversely, in the *APP/PSEN1* transgenic model, heterozygosity for the *Cd2ap* null allele had the opposite effect, leading to a decreased $A\beta_{42}/A\beta_{40}$ ratio [27], consistent with protection. Interestingly, *APP/PS1* mice also manifest decreased paired-pulse facilitation [66]; therefore, our finding of increased facilitation in *Cd2ap*^{+/-} mice may also be interpreted as potentially protective. However, other *Cd2ap* loss-of-function phenotypes are more difficult to reconcile, particularly the haploinsufficient requirement for visual discrimination learning.

Given its broad expression pattern and potential impact in many cell types in the brain and other tissues, it is unlikely that the action of CD2AP in AD pathogenesis can be precisely mapped to a single time and place. Instead, it is possible that CD2AP—and perhaps other AD risk genes—have distributed impacts in multiple cell types, different stages of disease, and with conflicting implications for risk versus protection. In sum, systematic functional dissection will be essential to define the requirements of each gene implicated in AD risk, both to inform an understanding of disease mechanisms as well as the full impact of potential therapies. Our work thus reveals the requirements for CD2AP in the mammalian brain and highlights important links to synaptic and proteostatic mechanisms with relevance to AD.

Materials and methods

Mouse strains

Mice were treated in compliance with US Department of Health and Human service and the Institutional Animal Care and Use Committee (IACUC). All procedures to maintain and use these mice were approved by IACUC for Baylor College of Medicine under protocol number AN5596. All mice were maintained on a 12-hour light-dark cycle and were provided with water and standard rodent diet *ad libitum*. We used both male and female mice in our studies. The following mouse lines were used in this study: wildtype C57BL/6 (JAX:000664), germline *Cd2ap* knockout (JAX:008907) [16] and germline *Cd2ap* knockout (MGI:6257815), nestin-Cre (JAX:003771), Cas9 (JAX:028239), and conditional *Cd2ap* knockout strain generated as part of this work (below). All mice were maintained on a C57BL/6 background. The *Cd2ap* knockout (MGI:6257815) allele, which was obtained from the Knockout Mouse Phenotyping Project (KOMP2), was used only in the behavioral touchscreen testing. Otherwise, the JAX:008907 *Cd2ap* germline knockout allele was used in all

other experiments involving germline *Cd2ap* knockout mice. The germline *Cd2ap* knockout alleles are based on targeted deletions of either exon 2 (JAX:008907) or exon 5 (MGI:6257815). *Cd2ap* conditional knockout mice were generated using cell-type-specific Cre-mediated deletion of the *Cd2ap* gene, as a service of the Augusta University Genome Editing Core. The target construct was designed by introducing loxP sites flanking *Cd2ap* exon 2, which encodes the first SRC homology 3 (SH3) domain and is the same exon that was targeted in the development of the germline *Cd2ap* knockout [16]. *Cd2ap* conditional knockout mice were generated by crossing *Cd2ap*^{lox/lox} mice with *nestin-cre* mice to obtain *Cd2ap*^{lox/lox};Nestin-Cre (*Cd2ap*^{ff};Nes-Cre) experimental mice. The Augusta Genome editing core also generated a *Cd2ap-HaloTag* knock-in mouse strain (C-terminal HaloTag). However, we were unable to confirm specific expression of this reporter, and the strain was therefore not used further, but is available upon request.

Mouse breeding schemes

We used the following breeding scheme to generate mice used in behavioral experiments on conditional *Cd2ap* knockout mice: *Cd2ap*^{lox/lox};Nestin-Cre male x *Cd2ap*^{lox/lox} female, which produced co-housed *Cd2ap*^{ff} and *Cd2ap*^{ff};Nes-Cre littermates. We used the following breeding scheme to generate germline *Cd2ap* knockout mice (JAX:008907) for all other *in vivo* experiments: *Cd2ap*^{+/-} male x *Cd2ap*^{+/-} female, which produced co-housed litters of *Cd2ap*^{+/+} ("WT"), *Cd2ap*^{+/-}, and *Cd2ap*^{-/-} mice. To generate germline *Cd2ap* knockout mice (MGI:6257815) used in the touchscreen assay, litters from a separate pool of WT and *Cd2ap*^{+/-} breeders were used. This is standard practice for the Knockout Mouse Phenotyping Project (KOMP2) and International Mouse Phenotyping Consortium (IMPC), through which touchscreen testing was completed. We thus cannot exclude litter effects as a potential source of variability that could account for any of the positive or negative results of the touchscreen assay. However, all mice (WT and experimental) were tested at the same time.

Histology and immunohistochemistry

Mice were deeply anesthetized using isoflurane and transcardially perfused with 10 ml of 1× phosphate-buffered saline (PBS; pH 7.35) followed by 10 ml of 4% paraformaldehyde (PFA; Electron Microscopy Sciences catalog # 15710) diluted in PBS. Brains were immersion fixed at 4°C for 12 to 48 h in 4% PFA and then transferred to 30% sucrose for cryoprotection overnight. Brains were then embedded in Tissue-Tek O.C.T. compound (Sakura Finetek United States catalog # 4583) and sectioned into ≤ 40- μ m sections on a cryostat (Leica CM1860). Free-floating tissue sections were placed into PBS immediately for immunohistochemistry (IHC).

For staining of synaptic proteins (PSD95 and Synapsin), brains were 'flash-frozen' in liquid nitrogen immediately after cardiac perfusion of mice with 10 ml of chilled PBS. Brains were then embedded in O.C.T., sliced into ≤ 30- μ m sections, and directly mounted onto glass slides (VWR catalog # 16005-108). Slides were immersion fixed in 4% PFA for 5 min before staining. All brain sections were blocked for 1 h at room temperature (RT) in 4% goat serum blocking solution made in 0.2% PBS-T (0.2% Triton-X 100 in PBS, pH 7.35) and then incubated in primary antibody diluted in blocking solution over-night at 4°C. Following three washes in 0.1% PBS-T (0.1% Triton-X 100 in PBS, pH 7.35) (15 min/wash at RT) slices were incubated in secondary antibody diluted in blocking solution for 2 h at RT. Slices were washed (three 15 min washes in 0.1% PBS-T at RT) and mounted using DAPI Fluoromount-G (SouthernBiotech catalog # 0100-20).

For immunohistochemistry of cultured neurons, culture media was aspirated from the wells and replaced with equal volume of warm 4% PFA/0.2M sucrose/1X PBS and incubated for 10 min at RT. Fixative was aspirated from wells and replaced with equal volume of 0.1% PBS-T and incubated for 10 min at RT. PBS-T solution was then replaced with a PBS wash, and the fixed cells were blocked for 1 h at RT in 2% goat serum blocking solution made in 0.01% PBS-T, and then incubated in primary antibody diluted in PBS + 1% goat serum over-night at 4°C. Following three washes in PBS + 1% goat serum (15 min/wash at RT), the cells were incubated in secondary antibody diluted in PBS + 1% goat serum for 2 h at RT, washed, and mounted using DAPI Fluoromount-G.

For Golgi-Cox staining, 37- to 41-day-old animals were euthanized with deep anesthesia in isoflurane chamber and perfused transcardially with 0.9% Sodium Chloride. The brains were dissected out and processed for a modified Golgi-Cox staining as described by the manufacturer of the FD Rapid GolgiStain™ Kit (FD NeuroTechnologies PK401), at the coronal section thickness of 200 μm.

Immunoblotting

Mice were euthanized with isoflurane followed by cervical dislocation. Hippocampal, cortex, or whole brain samples were dissected quickly on ice. Tissue was flash-frozen in liquid nitrogen and stored at -80°C. For immunoblotting, tissue was first lysed in RIPA Lysis and Extraction Buffer (Thermo Fisher catalog # 89900) prepared with protease inhibitor (GenDepot catalog # P3100-005). Each sample was placed in a test tube with 300 μl (for hippocampus) or 500 μl (for cortex, whole brain, and kidney) lysis buffer and homogenized using a pestle. For lysis of kidneys, samples were incubated in lysis buffer on ice for 10 min before homogenization. For lysis of cultured neurons, culture media was first aspirated from wells (~600 000 cells/well in a 6-well plate) and replaced with lysis buffer. Cells were then scraped, and the lysate transferred into a new tube. Both tissue and cultured cells lysates were spun down at the maximum speed at 4°C for 20 min. The supernatant was then transferred into a new test tube and spun again using the same settings. The protein concentration of the final lysate was calculated using the Pierce BCA Protein Assay Kit (Thermo Scientific catalog # 23225) and FLUOstar Optima microplate reader (BMG Labtech). The concentration of samples was normalized using Prism 9 and Excel, such that all samples had equal protein amount. Loading samples were made by mixing the same amount of protein from each lysate with 2X Laemmli sample buffer (Bio-Rad catalog # 1610737) with 5% b-mercaptoethanol. Loading samples were heated at 95°C for 5 min, followed by centrifugation at 15 000 rpm for 10 min. Samples were loaded at 15 μg into pre-cast 4 to 12% Bis-Tris protein gels (Invitrogen). Running buffer was 1× MOPS SDS (Invitrogen). Gels were transferred onto PVDF membrane (Millipore catalog # IPVH00010) on ice in 1× tris-glycine-sodium dodecyl sulfate transfer buffer with 20% methanol. Membranes were blocked with 5% bovine serum albumin (BSA) (Sigma catalog # A3294-100G) in tris-buffered saline with 0.1% Tween® 20 (TBST). TBST was used for all washing steps. Primary antibody incubations were performed overnight at 4 °C, and all secondary antibody incubation were 2 hours-long at RT. Primary antibodies were diluted in 5% BSA and secondary antibodies were diluted in TBST. After three washes, blots were developed using ECL (PerkinElmer catalog # NEL120001EA) for chemiluminescence and imaged using ChemiDoc MP Imaging System (BIO RAD) equipped with Image Lab Touch v2.4.0.03 software (BIO RAD). Western blot images were quantified using FIJI (ImageJ) 2.1.0/1.53c software. Raw data from

FIJI were imported into Excel, then into GraphPad Prism 9 software for graphing and statistical analysis.

Antibodies and dyes

The following antibodies were used for IHC and Western blot (WB) experiments: rabbit anti-CD2AP (IHC 1:2000, WB 1:200) (affinity purified, custom-made polyclonal antibody; validated using homozygous *Cd2ap* KO mouse brain tissue as the negative control (Figs 1A and S1A), chicken anti-MAP2 (IHC 1:750 on brain slices and 1:500 on fixed cultured cells, Abcam catalog # ab5392), mouse anti-NeuN (IHC 1:500, Sigma-Aldrich catalog # MAB377), mouse anti-PSD95 (IHC 1:500, WB 1:1000, NeuroMab-UC Davis catalog # 75-028), guinea pig anti-Synapsin (IHC 1:250, Synaptic Systems catalog # 106004), mouse anti-Synapsin (WB 1:100, Developmental Studies Hybridoma Bank-University of Iowa 3C11 anti SYNORF1 clone), mouse anti-Actin (WB 1:1000, Sigma-Aldrich catalog # MAB1501), and mouse anti-Tubulin (WB 1:1000, Sigma-Aldrich catalog # T6199). A new CD2AP antibody was generated by Biosynth, Inc. Rabbits were immunized with a peptide consisting of amino acids 597–610 of CD2AP (ALKKDHGKELEKLR-NH2) in Freund's adjuvant. Notably, the antigen sequence used in making the custom CD2AP antibody did not match the sequence of any protein other than CD2AP [89]. To limit potential non-specific binding of the custom-made antibody, the antibody was pre-absorbed using mouse *Cd2ap*^{-/-} brain tissue before use in IHC and WB. For pre-absorption, 400 μl of the purified antibody was incubated with 2 cryo-preserved *Cd2ap*^{-/-} brain tissue slices in 1 well of a 24-well plate for 4 h at 4 °C. The following secondary antibodies were used for fluorescence IHC: goat anti-mouse, anti-rabbit, anti-chicken, or anti-guinea pig antibodies conjugated to AlexaFluor-488, -546, -555, and -647 fluorophores (all 1:1000, Invitrogen). The following secondary antibodies were used for WB: goat anti-mouse or anti-rabbit IgG (H + L) antibodies conjugated to horseradish peroxidase (all 1:5000, Invitrogen). For actin staining in cultured neurons, we used a fluorescent-conjugated rhodamine phalloidin dye (Invitrogen catalog # R415) following manufacturer's protocol.

Microscopy and imaging

Images of fluorescent staining on brain slices and on primary cultured neurons were obtained using Leica LAS X software and the following microscopes: Leica confocal SP8 equipped with either a 10×/0.40 NA or 20×/0.75 NA dry objective, or a 63×/1.40 NA or 100×/1.40 NA oil objective; Leica MICA, equipped with a 10×/0.32 NA (dry), 20×/0.75 NA (dry), or 63×/1.20 NA (water) objective. All immunofluorescence images were processed using Imaris version 9.7.2 (Bitplane Software) or FIJI 2.1.0/1.53c. (ImageJ). Neuronal and dendritic morphology analyses on cultured neuron images were completed in Imaris as previously described [90]. Briefly, we used Filament tracer extension to trace dendritic arbors of cultured neurons using the autopath function with thinnest diameter set to 1.00 μm. Dendritic spines were detected using the Filament tool with spine length empirically determined to be < 3μm. Spine types were classified using the Filament tool and the following criteria: mushroom (mean_width(head) < mean_width(neck), spine length < 2.5μm), stubby (spine length < 0.75μm), long thin (mean_width(head) = mean_width(neck)). Sholl analysis was completed using the Filament Sholl Analysis XTension.

For quantification of dendritic trees and spine density, CA1 pyramidal neurons that fulfill all the following criteria were selected for neuron reconstruction: 1. somas reside in the middle 50 μm of the 200 μm section 2. impregnated in their entirety 3. have continuous and complete dendritic trees

throughout Stratum Oriens (SO) and Stratum Radiatum (SR), and reaching into Stratum Lacunosum-Moleculare (SLM). Three-dimensional neuron reconstruction was performed using 100× oil-immersion objective of a Zeiss widefield apotome microscope with Neurolucida software (MBF Bioscience). Basal dendrites were traced for their entirety, and apical dendrites were traced up to ~350 μm from the somas (i.e. the entirety in SR and the beginning of SLM). For dendritic branching analysis, 9 neurons were reconstructed for each experimental group (from 4 wildtype controls, 4 *Cd2ap*^{+/-}, and 2 *Cd2ap*^{-/-} animals). Structural and spatial analysis (including dendritic length, branching points, and Sholl analysis) for apical and basal dendritic trees were performed with Neurolucida Explorer software (MBF Bioscience). For dendritic spine imaging, 100× oil-immersion objective of Nikon microscope was used. CA1 pyramidal neurons were selected based on the same criteria as above. In each neuron, 2 main apical dendritic segments (100~200 μm from soma) and 3 apical oblique dendritic segments (120~240 μm from soma) within the Stratum Radiatum, and 3 basal dendritic segments within the Stratum Oriens were randomly selected for imaging and quantification. These segments are evenly impregnated in their entirety and at least 20 μm in length. All protrusions (whether thin or stubby, with or without mushroom-like expansions) were counted as spines if they were in direct continuity with the dendritic shaft. 3~6 neurons were analyzed for each group, resulting in 11~18 neurons per group. Spine densities were calculated as mean numbers of spines per 10 micrometer dendritic segment per neuron. Spines located on main apical dendrites, on apical oblique dendrites, and on basal dendrites were analyzed separately.

Proteasome activity assay

In vitro proteasome activity assay was carried out using the 20S Proteasome Activity Assay kit (Sigma-Aldrich catalog # APT280) and following the manufacturer protocol. Briefly, media was aspirated from wells (~600 000 cells/well) and replaced with lysis buffer. Cells were scraped and lysed, and sample protein concentration was quantified and normalized using the Pierce BCA Protein Assay Kit as described above for Immunoblotting. Sample lysates of equal protein amount were added to an assay mixture of proteasome substrate (Suc-LVY-AMC), assay buffer and water (adding up to 100 μl) and then incubated for 2 h at 37 °C in a 96-well plate. Fluorescence intensity was read using a 380/460 nm filter set on FLUOstar Optima microplate reader (BMG Labtech).

Cd2ap expression analysis

Cd2ap expression was evaluated using reverse transcription polymerase chain reaction (PCR) as previously described [91–93]. Briefly, mice were euthanized with isoflurane followed by cervical dislocation and their hippocampi and cortices rapidly dissected on ice. Tissue was homogenized using a pellet pestle and RNA was extracted using 15 μl Trizol (Thermo Fisher catalog # 15596026) per 1 mg tissue. Chloroform was added at 1/5 volume of Trizol for 5 min incubation at RT. Samples were spun at 12 000 × g for 15 min at 4°C. Aqueous phase was pipetted into a new tube, 70% of aqueous phase by volume of isopropanol was added, and the mixture was incubated at RT for 10 min. Samples were then centrifuged at max speed for 5 min at 4°C, and the supernatant was discarded. Pellets were washed with ~500 μl 70% cold ethanol and centrifuged at 7500 × g for 10 min at 4°C. Ethanol was removed and pellets were resuspended in nuclease-free water. RNA was quantified using a NanoDrop (Wilmington, DE) and then

DNase-digested following manufacturer's protocol (Invitrogen catalog # 18068015). cDNA was synthesized using the GoScript Reverse Transcription Kit (Promega catalog # A5000) following manufacturer's protocol. Negative controls contained no reverse transcriptase. Quantitative PCR was performed using SYBR Green master mix (Thermo Fisher catalog # K0221) in 96-well plates (Applied biosystems catalog # N8010560). The following PCR primers were used: Primer pair 1: f-TCCGAGTTGGGGAAATCATCA and r-TGTCTCTCGCTTAATTTCCCTTAACA. Primer pair 2: f-ACTA CAGGAAGAAGGATGGCT and r-TGTCTCTCGCTTAATTTCCCTTAAC. Applied Biosystems Design and Analysis v2.6.0 software (Thermo Fisher) was used for data analysis.

Primary neuronal cultures

Primary neuron cultures were prepared from postnatal day 0 (P0) mouse pups as previously described [94]. Briefly, pups were euthanized by decapitation and their cortices were dissected under a microscope in Hanks' Balanced Salt Solution (Invitrogen catalog # 14110-172). Dissected cortices were placed in Eppendorf tubes containing complete Neurobasal (CNB) media on a 37°C shaker at 1000 rpm before dissociation. The recipe for CNB was Neurobasal media (NB) (Invitrogen catalog # 21103049) with 2% B-27 supplement (Invitrogen catalog # 17504-044), 2 mM GlutaMax (Invitrogen catalog # 35050-061), and 0.2× Pen/Strep antibiotics (Invitrogen catalog # 15140-122). The neurons were dissociated (45 min at 1000 rpm on 37°C shaker) before addition of inhibitor (5 min at 1000 rpm on 37°C shaker) using Papain Dissociation System Kit (Worthington catalog # LK003153) solutions prepared per manufacturer's instructions. The neurons were then plated at a density of 100 000–600 000/well (lower cell count was used in imaging experiments, and higher cell count was used for immunoblotting) on 24-well plates or 4–8 well glass slides (Millipore catalog # PEZGS0816) coated with poly-D-lysine (0.1 mg/ml) (Sigma catalog # P6407) and maintained in CNB.

For *in vitro* knockout of *Cd2ap*, we used Cas9 mice [95], which express Cas9 at the Hipp11 locus, allowing constitutive expression of Cas9 nuclease and CRISPR-mediated knockout of *Cd2ap*. Cas9 neurons were transfected on DIV3 (0.3 μl virus in 500 μl of media/well in a 24-well plate) using either of two viruses: AAV-U6-sgRNA *Cd2ap*-Efl1a-tdTomato (knockout) or AAV-U6-sgRNA-Control-EF1a-EGFP (control). Experimental/knockout AAV expressed two sgRNAs targeting *Cd2ap*, under the U6 promoter, and tdTomato under the Efl1-alpha promoter. The sgRNA sequences were CTGGAGCAGTGTACCCAAAG and AACTTCCAGTAGTAAACAG. Control AAV expressed guide sequences targeting LacZ under the U6 promoter and EGFP under the Efl1-alpha promoter. Control sgRNA sequences were AACCCGTGGTTCGGCTTACGG and CATCGGGCAAATAATATCGG. The serotype of both AAVs was DJ8. Packaging into AAV was performed by the Neuroconnectivity Core at the Jan and Dan Duncan Neurological Research Institute.

Behavioral studies

Excluding touchscreen assays, all testing was completed on “young” (14–16-weeks-old at start of testing) and “aged” mice (50–54-weeks-old at start of testing). The behavioral battery took 1–3 weeks to complete. Unless otherwise stated, tests were performed with ±60 dB white noise and under 150–200 lux illumination and data were collected using computer-operated apparatus via ANY-Maze 6.2 (Stoelting Co.) software. All mouse behavioral testing was completed at the Animal Behavior Core at the Duncan Neurological Research Institute.

Elevated plus maze

Mouse anxiety was evaluated as previously described [96] with some adjustments. Briefly, mice were placed in the center (facing an open arm) of a plastic plus-shaped platform maze that was elevated above the floor. Two opposite arms (25 cm × 7.5 cm) of the maze were walled with 15-cm-high walls, and the other two arms were open. Mice were able to move freely and choose to enter the different arms of the maze during 10 min. Their activity was traced automatically by ANY-Maze.

Y-maze

Mouse working memory was evaluated in Y-maze as previously described [97] with some adjustments. Briefly, mice were placed in the center of a plastic Y-shaped platform maze that was elevated above the floor. All three arms of the maze were walled (15-cm-high walls). Testing was performed at regular room 700–750 lux for 10 min. Mice were able to move freely and choose to enter the different arms of the maze. Their activity was traced automatically by ANY-Maze. Spontaneous alteration (% alteration) was calculated as $(\text{Alternate arm entry} / \text{total arm entry}) \times 100$, where *Alternate arm entry* was the number of times the mouse consecutively entered three different arms of the Y-maze.

Open field assay

Mouse activity and anxiety levels were evaluated in as previously described [98]. Briefly, mice were placed in the center of the glass-walled chamber (40 × 40 × 30 cm) and their activity was measured by photobeams connected to a computer operated Digiscan optical animal activity software (AccuScan, Columbus, OH, United States) for 30 min.

Novel object recognition

Mouse recognition memory was tested as previously described [99] over 2 days. Briefly, on both days, the mice were placed in a habituation arena for 5 min before 5 min-long testing. The habituation arena and the testing arena were two identical, large, empty rodent cages. On day 1, the testing arena contained two identical objects. On day 2, the testing arena contained one object from the previous day and one novel object. Both objects were two ~12 cm tall Lego objects, either identical (day 1), or differing in color pattern and shape (day 2). The amount of time spent exploring each object (approaching the object closely while being oriented towards it, sniffing the object, or touching the object) was quantified manually via ANY-Maze. The preference index was calculated as $\text{time spent exploring novel object} / [(\text{total time spent exploring both familiar and novel object}) \times 100]$, as previously described [100].

Fear conditioning

Mouse freezing data in fear conditioning were acquired automatically using FreezeFrame4 software (Actimetrics/Coulbourn Instruments). On day 1 (“training”), mice were placed into sound-attenuated chambers for 2 min before a sound (30 s, 85 ± 2 dB) (conditioned stimulus) came on and was immediately followed by a foot shock (2 s, 1.0 mA) (unconditioned stimulus). This conditioning pattern was repeated once. 24 h after the conditioning, mice were placed in the same environment and observed for 5 min (“context”). One hour after completion of the context paradigm, the mice were placed back in the chamber but with the environment changed (bedding was removed from transfer cages and testing chambers were modified with a plastic cover on the chamber floor, vanilla syrup behind a plastic wall, and the room now had red overhead lighting) for the final “cued fear” paradigm.

Mice were in the modified chamber for 3 min before the sound (conditioned stimulus) came on stayed on for 3 min.

Hot plate

Mice were tested for pain recognition as previously described [98]. Briefly, mice were placed in a Hot-Plate Analgesia Meter (Columbus Instruments), pre-heated to 55 C. Their latency to respond to heat was recorded manually and served as a functional readout of pain recognition. Responses included hindlimb licking, shaking, or twitching.

Touchscreen assays

WT and *Cd2ap*^{+/-} mice in this assay were tested between 2–3-months-of-age. For the visual discrimination task, we used the Bussey-Saksida touchscreen operant system (Campden Instruments/Lafayette Instrument Company, Lafayette, Indiana). These trapezoidal touchscreen boxes were fitted with screens containing a two-hole mask, measuring 7 × 7 cm. Visual images were presented on each of the 2 holes, one of which was correct (S+) and the other incorrect (S–). When the mouse nose-poked the correct image the food reward (strawberry milkshake, Ensure®) was presented through plastic tubing regulated by a peristaltic pump, along with the illumination of the tray light and a tone. If the animal chose an incorrect response, they received no food reward, and the house light was turned on. Mice were first acclimated to the chambers, following which they were trained to touch the screen through the ‘Initial touch’ module. This was followed by the ‘Must touch’ module where stimuli were displayed randomly on the screen one at a time and the animal must touch the stimulus to elicit a tone/food response and complete 30 trials in 60 min to reach criterion. Animals then entered the “must initiate” module, where there was free delivery of food, and the tray light would be turned on. Once the mouse nose-poked and exited the reward tray, the stimulus was presented on the screen. One stimulus was presented at a time, with the other side left blank. The mouse had to touch the stimulus to elicit tone/food response. The duration of the module was 60 min or 30 correct trials, whichever occurred first. The mice then advanced to the “punish incorrect” module, in which incorrect responses are paired with illumination of the house light and no reward as a negative reinforcement. The mice were presented with 30 trials and had to achieve 23/30 (77%) correct trials in 30 min for 2 days in a row to advance to the next module. The next module was pairwise discrimination, the visual discrimination task. In each trial there were two stimuli, of which one was associated with a food reward and the other with negative reinforcement. Mice had to complete 30 trials in < 60 min and achieve at least 24/30 (80%) correct trials.

Electrophysiology

All electrophysiological recordings were performed in acute coronal brain slices from 5 to 8-week old animals. For slice preparation, mice were anesthetized with isoflurane and perfused with cold artificial cerebrospinal fluid solution (ACSF). Brains were quickly removed, placed into sucrose-based cutting solution, cut at 300 micrometer thickness using a Leica VT1200 vibratome, and prepared for recordings as is standard for our lab and previously described [90]. The recipe for ACSF was as follows: 125 mM NaCl, 2.5 mM KCl, 1.25 mM NaH₂PO₄, 2 mM CaCl₂, 1 mM MgCl₂, 10 mM glucose, and 25 mM NaHCO₃. The recipe for the cutting solution (pH 7.35) was as follows (in mM): 87 NaCl, 2.5 KCl, 1.25 NaH₂PO₄, 0.5 CaCl₂, 7 MgCl₂–6H₂O, 13 ascorbic acid, 75 sucrose, 10 glucose, and 25 NaHCO₃. Neurons were visualized using differential interference contrast (Olympus BX50WI) and

an optiMOS camera (QImaging) via Micro-Manager version 1.4.22 software (University of California at San Francisco). Axon Multi-Clamp 700B amplifier digitized at 10 kHz (Axon Digidata 1440A) and pCLAMP software 10.7.0 were used for recordings. Recording electrodes (3–5 M Ω) were prepared from borosilicate glass microcapillaries (outer diameter 1.5 mm) with a micropipette puller (Sutter Instruments). The following recipe was used for the internal solution (in mM): 120 Cs-MeSO₄, 10 CsCl, 2 MgCl₂, 4 ATP-Mg, 0.5 GTP-Na, 10 phosphocreatine-di-Na, 1 EGTA, and 20 HEPES; pH was adjusted to 7.3 with CsOH, and the osmolarity was adjusted to 305 mOsm/l with CsMeSO₄. Access resistance was monitored throughout the recordings and was maintained at 10–20 M Ω (up to 30 M Ω was considered acceptable). Miniature excitatory post-synaptic currents (mEPSCs) were recorded from CA1 pyramidal neurons in the presence of tetrodotoxin. mEPSCs data were analyzed using Synaptosoft Mini Analysis 6.0.7 software, with the detection threshold at 4 pA. Recorded traces were observed by eye and artifacts were corrected as necessary. The following electrode internal solution (in mM) was used in current clamp recordings: 110 K-gluconate, 10 KCl, 4 ATP-Mg, 0.5 GTP-Na, 10 Phosphocreatine-di-Na, 1 EGTA, 10 HEPES; pH was adjusted to 7.3 with KOH, the osmolarity to 305 mOsm/l with K-gluconate. After obtaining a whole cell seal, baseline activity was monitored for a few minutes without current injection to ensure stability. Series of hyper- and depolarizing current injection steps/ramps were then applied to analyze the firing mode, the rheobase, and threshold. Data were analyzed using Clampfit 10.7.0.3 (Molecular Devices) software. Hippocampus field recordings were obtained as previously described [101]. Briefly, CA1 was stimulated on Schaffer collaterals using platinum/iridium parallel bipolar electrode (1 M Ω ; 75 μ m tip separation) (Microprobes, Gaithersburg, MD, United States). The recording electrode (2 M Ω) was a glass pipette filled with ACSF. For the paired pulse facilitation recordings two fEPSP were evoked with the two stimulus pulses of the same current magnitude as above, separated by 50, 100, 200 or 500 ms. The fEPSP we analyzed offline for the rising slope, using Clampfit 10.7.0.3 (Molecular Devices).

Proteomics

Mice were euthanized and hippocampi for proteomics were dissected, flash frozen, and stored at –80°C until use as described above. Tandem mass tag mass-spectrometry proteomics was performed as previously described [102] for *Cd2ap*^{–/–}, *Cd2ap*^{+/-}, and wildtype hippocampi. 5 right hemisphere hippocampi from 34–37-day-old (4.5–5-week-old) mice were used per genotype (one hippocampus/mouse). All samples were processed as a single batch. Protein database search and protein quantification was performed with Proteome Discover using the mouse Uniprot database (August 2020 with 91413 entries). The entire protein dataset included 125719 unique peptides, mapping to 9605 unique protein isoforms. Mapping of Uniprot IDs to Entrez IDs was performed using the R package AnnotationDbi v.1.64.1. Protein isoforms containing missing values were excluded and protein intensity values mapping to the same Entrez gene ID were summed, resulting in 8478 unique proteins. The data was log₂ transformed to allow for the application of parametric statistics. For differential expression, t-tests were used to compare the normalized abundance levels between control and *Cd2ap*^{–/–} or *Cd2ap*^{+/-} KO mice for each selected gene. A cutoff of P-value < 0.05 was set to select differentially expressed proteins (DEPs). Volcano plots were plotted using the R package ggplot2 v. 3.4.4. Overrepresentation analysis (ORA) of differentially expressed gene sets was completed using the R implementation of

gProfiler (gprofiler2 v. 0.2.2) [103] and online SynGO (<https://www.syngoportal.org/>) [104]. SynGO requires the conversion of mouse genes to human gene orthologs before running the enrichment analyses. The gene conversion was performed using SynGO suggested tool (<https://www.syngoportal.org/convert>). For both analyses, a false discovery rate (FDR) < 0.05 was the threshold for significance. From the gProfiler results, the Gene Ontology (GO) database was used for querying representative and proteasome-related genes and ontology terms. Bar graphs were plotted using GraphPad Prism v. 10.0.2. Venn diagrams overlaps were calculated using nVenn (<https://degradome.uniovi.es/cgi-bin/nVenn/nVenn.cgi>) and Fisher test significance of the overlaps was calculated using R. The background of proteins used to calculate overlap significance was all proteins from the differential expression analysis (n = 8478). The full proteomics dataset (log₂-transformed/normalized) is available in the Supplemental Data File along with associated Metadata (Table S4).

Human brain eQTL analysis

CD2AP eQTL analysis from single-nucleus RNA-seq of human brains was based on a recently published dataset [35]. In brief, single-nucleus RNA-seq libraries were prepared from 424 dorso-lateral prefrontal cortex (DLPFC) of the ROS/MAP cohort using 10 \times Genomics Single Cell 3' kit. Sequencing reads were processed and UMI count matrix was generated using Cell Ranger software (ver.6.0.0, 10 \times Genomics). Classification of cell types were performed by clustering cells by gene expression using the R package Seurat (ver. 4). “Pseudobulk” gene expression matrix was constructed by aggregating UMI counts of the same cell type of the same donor and normalizing them to the log₂ counts per million reads mapped (CPM) values. Genotyping was performed by whole genome sequencing and GATK. Mapping of cis-eQTL was performed using Matrix-eQTL (ver. 2.3) for SNP within 1 Mb from transcription start sites.

Statistics

Specific analysis methods are described with the corresponding experimental procedures (above). Sample size for all comparisons is included in each figure legend. Unless otherwise noted, the significance threshold for all analyses was set to P < 0.05 (two-tailed test) and all statistical analyses were performed using Prism 9 version 9.5.0 (GraphPad) software. Outlier values in the data for the electrophysiology (Fig. 4) and behavioral analysis (Fig. 5) were identified and excluded using the ROUT test in Prism 9 with default parameters (Q = 1%).

Acknowledgements

We would like to thank Andrey Shaw, Lunhui (Frank) Lin, and Jimmy Holder for sharing mouse strains. We are also grateful to Hui Ye and Hilary Chester for assistance with cell culture maintenance and Brandon Pekarek for help with molecular biology. We also thank Rodney Samaco for consultation regarding the mouse behavioral experiments.

Funding

This work was funded by NIH grants, including R01AG050631 (Shulman/Arenkiel), U01AG072439 (Shulman), and U01AG072572 (De Jager/St George-Hyslop). We also received funding from the NIH Accelerating Medicines Partnership (AMP)-AD consortium, including U01AG061357 (Shulman/Seyfried), RF1AG057473 (De Jager/Bennett), and U01AG061356 (De Jager/Bennett). Dr Ojelade was supported by the Postdoctoral Enrichment Program Award

from the Burroughs Wellcome Fund (BWF-1017399) and an Alzheimer's Association fellowship (AARFD-16-442630). Research reported in this publication was supported by the Eunice Kennedy Shriver National Institute of Child Health & Human Development of the National Institutes of Health under Award Number P50HD103555 for use of the Microscopy and Animal Phenotyping & Preclinical Outcomes Core facilities. The content is solely the responsibility of the authors and does not necessarily represent the official views of the Eunice Kennedy Shriver National Institute of Child Health & Human Development of the National Institutes of Health.

Supplementary data

Supplementary data is available at HMG Journal online.

Conflict of interest statement: None declared.

References

1. Spires-Jones TL, Hyman BT. The intersection of amyloid beta and tau at synapses in Alzheimer's disease. *Neuron* 2014;**82**: 756–771.
2. Bellenguez C, Küçükali F, Jansen IE. et al. New insights into the genetic etiology of Alzheimer's disease and related dementias. *Nat Genet* 2022;**54**:412–436.
3. Kunkle BW, Grenier-Boley B, Sims R. et al. Genetic meta-analysis of diagnosed Alzheimer's disease identifies new risk loci and implicates A β , tau, immunity and lipid processing. *Nat Genet* 2019;**51**:414–430.
4. Jansen IE, Savage JE, Watanabe K. et al. Genome-wide meta-analysis identifies new loci and functional pathways influencing Alzheimer's disease risk. *Nat Genet* 2019;**51**:404–413.
5. Onos KD, Sukoff Rizzo SJ, Howell GR. et al. Toward more predictive genetic mouse models of Alzheimer's disease. *Brain Res Bull* 2016;**122**:1–11.
6. Pimenova AA, Raj T, Goate AM. Untangling genetic risk for Alzheimer's disease. *Biol Psychiatry* 2018;**83**:300–310.
7. Braak H, Alafuzoff I, Arzberger T. et al. Staging of Alzheimer disease-associated neurofibrillary pathology using paraffin sections and immunocytochemistry. *Acta Neuropathol* 2006;**112**: 389–404.
8. Lace G, Savva GM, Forster G. et al. Hippocampal tau pathology is related to neuroanatomical connections: an ageing population-based study. *Brain* 2009;**132**:1324–1334.
9. Ojelade SA, Lee TV, Giagtzoglou N. et al. Cindr, the drosophila homolog of the CD2AP Alzheimer's disease risk gene, is required for synaptic transmission and Proteostasis. *Cell Rep* 2019;**28**:1799–1813.e5.
10. Kirsch KH, Georgescu M-M, Ishimaru S. et al. CMS: an adapter molecule involved in cytoskeletal rearrangements. *PNAS* 1999;**96**:6211–6216.
11. Dustin ML, Olszowy MW, Holdorf AD. et al. A novel adaptor protein orchestrates receptor patterning and cytoskeletal polarity in T-cell contacts. *Cell* 1998;**94**:667–677.
12. Hollingworth P, Harold D, Sims R. et al. Common variants at ABCA7, MS4A6A/MS4A4E, EPHA1, CD33 and CD2AP are associated with Alzheimer's disease. *Nat Genet* 2011;**43**:429–435.
13. Kim JM, Wu H, Green G. et al. CD2-associated protein Haploinsufficiency is linked to glomerular disease susceptibility. *Science* 2003;**300**:1298–1300.
14. Tsvetkov D, Hohmann M, Anistan YM. et al. A CD2AP mutation associated with focal segmental Glomerulosclerosis in young adulthood. *Clin Med Insights Case Rep* 2016;**9**:15–19.
15. Gigante M, Pontrelli P, Montemurno E. et al. CD2AP mutations are associated with sporadic nephrotic syndrome and focal segmental glomerulosclerosis (FSGS). *Nephrol Dial Transplant* 2009;**24**:1858–1864.
16. Shih NY, Li J, Karpitskii V. et al. Congenital nephrotic syndrome in mice lacking CD2-associated protein. *Science* 1999;**286**: 312–315.
17. Harrison BJ, Venkat G, Lamb JL. et al. The adaptor protein CD2AP is a coordinator of Neurotrophin Signaling-mediated axon arbor plasticity. *J Neurosci* 2016;**36**:4259–4275.
18. Li C, Ruotsalainen V, Tryggvason K. et al. CD2AP is expressed with nephrin in developing podocytes and is found widely in mature kidney and elsewhere. *Am J Physiol Renal Physiol* 2000;**279**:F785–F792.
19. Cochran JN, Rush T, Buckingham SC. et al. The Alzheimer's disease risk factor CD2AP maintains blood–brain barrier integrity. *Hum Mol Genet* 2015;**24**:6667–6674.
20. Lynch DK, Winata SC, Lyons RJ. et al. A cortactin-CD2-associated protein (CD2AP) complex provides a novel link between epidermal growth factor receptor endocytosis and the actin cytoskeleton. *J Biol Chem* 2003;**278**:21805–21813.
21. Johnson RI, Bao S, Cagan RL. Interactions between drosophila IgCAM adhesion receptors and cindr, the Cd2ap/Cin85 ortholog. *Dev Dyn* 2012;**241**:1933–1943.
22. Johnson RI, Seppa MJ, Cagan RL. The drosophila CD2AP/CIN85 orthologue Cindr regulates junctions and cytoskeleton dynamics during tissue patterning. *J Cell Biol* 2008;**180**:1191–1204.
23. Cormont M, Metón I, Mari M. et al. CD2AP/CMS regulates endosome morphology and traffic to the degradative pathway through its interaction with Rab4 and c-Cbl. *Traffic* 2003;**4**: 97–112.
24. Karch CM, Goate AM. Alzheimer's disease risk genes and mechanisms of disease pathogenesis. *Biol Psychiatry* 2015;**77**:43–51.
25. Shulman JM, Imboywa S, Giagtzoglou N. et al. Functional screening in drosophila identifies Alzheimer's disease susceptibility genes and implicates tau-mediated mechanisms. *Hum Mol Genet* 2014;**23**:870–877.
26. Ubelmann F, Burringha T, Salavessa L. et al. Bin1 and CD2AP polarise the endocytic generation of beta-amyloid. *EMBO Rep* 2017;**18**:102–122.
27. Liao F, Jiang H, Srivatsan S. et al. Effects of CD2-associated protein deficiency on amyloid- β in neuroblastoma cells and in an APP transgenic mouse model. *Mol Neurodegener* 2015;**10**:12.
28. Huttlin EL, Jedrychowski MP, Elias JE. et al. A tissue-specific atlas of mouse protein phosphorylation and expression. *Cell* 2010;**143**:1174–1189.
29. Mandyam CD. The interplay between the hippocampus and amygdala in regulating aberrant hippocampal neurogenesis during protracted abstinence from alcohol dependence. *Front Psychiatry* 2013;**4**:61.
30. Scharfman HE. The enigmatic mossy cell of the dentate gyrus. *Nat Rev Neurosci* 2016;**17**:562–575.
31. Amaral DG, Scharfman HE, Lavenex P. The dentate gyrus: fundamental neuroanatomical organization (dentate gyrus for dummies). *Prog Brain Res* 2007;**163**:3–22.
32. Mullen RJ, Buck CR, Smith AM. NeuN, a neuronal specific nuclear protein in vertebrates. *Development* 1992;**116**: 201–211.
33. Cho K-O, Hunt CA, Kennedy MB. The rat brain postsynaptic density fraction contains a homolog of the drosophila discs-large tumor suppressor protein. *Neuron* 1992;**9**:929–942.
34. De Camilli P, Benfenati F, Valtorta F. et al. The Synapsins. *Annu Rev Cell Biol* 1990;**6**:433–460.

35. Fujita M, Gao Z, Zeng L. *et al.* Cell-subtype specific effects of genetic variation in the aging and Alzheimer cortex. *Nat Genet* 2024;**56**:605–614.
36. Wightman DP, Jansen IE, Savage JE. *et al.* A genome-wide association study with 1,126,563 individuals identifies new risk loci for Alzheimer's disease. *Nat Genet* 2021;**53**:1276–1282.
37. Fiala JC, Spacek J, Harris KM. Dendritic spine pathology: cause or consequence of neurological disorders? *Brain Res Rev* 2002;**39**:29–54.
38. Kasai H, Matsuzaki M, Noguchi J. *et al.* Structure-stability-function relationships of dendritic spines. *Trends Neurosci* 2003;**26**:360–368.
39. Braak H, Braak E, Bohl J. Staging of Alzheimer-related cortical destruction. *Eur Neurol* 1993;**33**:403–408.
40. Regehr WG. Short-term presynaptic plasticity. *Cold Spring Harb Perspect Biol* 2012;**4**:a005702.
41. Tronche F, Kellendonk C, Kretz O. *et al.* Disruption of the glucocorticoid receptor gene in the nervous system results in reduced anxiety. *Nat Genet* 1999;**23**:99–103.
42. Groza T, Gomez FL, Mashhadi HH. *et al.* The international mouse phenotyping consortium: comprehensive knockout phenotyping underpinning the study of human disease. *Nucleic Acids Res* 2023;**51**:D1038–D1045.
43. Horner AE, Heath CJ, Hvoslef-Eide M. *et al.* The touchscreen operant platform for testing learning and memory in rats and mice. *Nat Protoc* 2013;**8**:1961–1984.
44. Mar AC, Horner AE, Nilsson SRO. *et al.* The touchscreen operant platform for assessing executive function in rats and mice. *Nat Protoc* 2013;**8**:1985–2005.
45. Bussey TJ, Padain TL, Skillings EA. *et al.* The touchscreen cognitive testing method for rodents: how to get the best out of your rat. *Learn Mem* 2008;**15**:516–523.
46. Romberg C, Mattson MP, Mughal MR. *et al.* Impaired attention in the 3xTgAD mouse model of Alzheimer's disease: rescue by donepezil (Aricept). *J Neurosci* 2011;**31**:3500–3507.
47. Leach PT, Crawley JN. Touchscreen learning deficits in Ube3a, Ts65Dn and Mecp2 mouse models of neurodevelopmental disorders with intellectual disabilities. *Genes Brain Behav* 2018;**17**:e12452.
48. Lein ES, Hawrylycz MJ, Ao N. *et al.* Genome-wide atlas of gene expression in the adult mouse brain. *Nature* 2007;**445**:168–176.
49. Meftah S, Gan J. Alzheimer's disease as a synaptopathy: evidence for dysfunction of synapses during disease progression. *Front Synaptic Neurosci* 2023;**15**:1129036.
50. Selkoe DJ. Alzheimer's disease is a synaptic failure. *Science* 2002;**298**:789–791.
51. Jacob CP, Koutsilieris E, Bartl J. *et al.* Alterations in expression of glutamatergic transporters and receptors in sporadic Alzheimer's disease. *J Alzheimers Dis* 2007;**11**:97–116.
52. Szabo MP, Mishra S, Knupp A. *et al.* The role of Alzheimer's disease risk genes in endolysosomal pathways. *Neurobiol Dis* 2022;**162**:105576.
53. Hegde AN. Ubiquitin-proteasome-mediated local protein degradation and synaptic plasticity. *Prog Neurobiol* 2004;**73**:311–357.
54. Speese SD, Trotta N, Rodesch CK. *et al.* The ubiquitin proteasome system acutely regulates presynaptic protein turnover and synaptic efficacy. *Curr Biol* 2003;**13**:899–910.
55. Karpova A, Mikhaylova M, Thomas U. *et al.* Involvement of protein synthesis and degradation in long-term potentiation of Schaffer collateral CA1 synapses. *J Neurosci* 2006;**26**:4949–4955.
56. Lehtonen S, Zhao F, Lehtonen E. CD2-associated protein directly interacts with the actin cytoskeleton. *Am J Physiol Renal Physiol* 2002;**283**:F734–F743.
57. Dillon C, Goda Y. The actin cytoskeleton: integrating form and function at the synapse. *Annu Rev Neurosci* 2005;**28**:25–55.
58. Goujon M, McWilliam H, Li W. *et al.* A new bioinformatics analysis tools framework at EMBL-EBI. *Nucleic Acids Res* 2010;**38**:W695–W699.
59. Sievers F, Wilm A, Dineen D. *et al.* Fast, scalable generation of high-quality protein multiple sequence alignments using Clustal Omega. *Mol Syst Biol* 2011;**7**:539.
60. Bateman A, Martin M-J, Orchard S. *et al.* UniProt: the universal protein knowledgebase in 2023. *Nucleic Acids Res* 2023;**51**:D523–D531.
61. Altschul SF, Gish W, Miller W. *et al.* Basic local alignment search tool. *J Mol Biol* 1990;**215**:403–410.
62. Shimokawa N, Haglund K, Hölter SM. *et al.* CIN85 regulates dopamine receptor endocytosis and governs behaviour in mice. *EMBO J* 2010;**29**:2421–2432.
63. Braun TP, Grossberg AJ, Veleva-Rotse BO. *et al.* Expression of myeloid differentiation factor 88 in neurons is not requisite for the induction of sickness behavior by interleukin-1 β . *J Neuroinflammation* 2012;**9**:229.
64. Teng E, Stefanacci L, Squire LR. *et al.* Contrasting effects on discrimination learning after hippocampal lesions and conjoint hippocampal-caudate lesions in monkeys. *J Neurosci* 2000;**20**:3853–3863.
65. Lénárt N, Szegedi V, Juhász G. *et al.* Increased tau phosphorylation and impaired presynaptic function in hypertriglyceridemic ApoB-100 transgenic mice. *PLoS One* 2012;**7**:e46007.
66. Sha S, Chaigneau T, Krantic S. Pre-symptomatic synaptic dysfunction and longitudinal decay of hippocampal synaptic function in APPS1 mouse model of Alzheimer's disease is sex-independent. *Brain Res Bull* 2023;**198**:36–49.
67. Benitez DP, Jiang S, Wood J. *et al.* Knock-in models related to Alzheimer's disease: synaptic transmission, plaques and the role of microglia. *Mol Neurodegener* 2021;**16**:47.
68. Šišková Z, Justus D, Kaneko H. *et al.* Dendritic structural degeneration is functionally linked to cellular Hyperexcitability in a mouse model of Alzheimer's disease. *Neuron* 2014;**84**:1023–1033.
69. Hoffmann NA, Dorostkar MM, Blumenstock S. *et al.* Impaired plasticity of cortical dendritic spines in P301S tau transgenic mice. *Acta Neuropathol Commun* 2013;**1**:82.
70. Upadhyaya SC, Hegde AN. Role of the ubiquitin proteasome system in Alzheimer's disease. *BMC Biochem* 2007;**8**:S12.
71. Piiipponiemi TO, Bragge T, Vauhkonen EE. *et al.* Acquisition and reversal of visual discrimination learning in APPSwDI/Nos2–/– (CVN) mice. *Neurosci Lett* 2017;**650**:126–133.
72. Hyde LA, Crnic LS. Age-related deficits in context discrimination learning in Ts65Dn mice that model down syndrome and Alzheimer's disease. *Behav Neurosci* 2001;**115**:1239–1246.
73. Spires-Jones T, Knafo S. Spines, plasticity, and cognition in Alzheimer's model mice. *Neural Plast* 2012;**2012**:319836.
74. Penzes P, Cahill ME, Jones KA. *et al.* Dendritic spine pathology in neuropsychiatric disorders. *Nat Neurosci* 2011;**14**:285–293.
75. Elder MK, Erdjument-Bromage H, Oliveira MM. *et al.* Age-dependent shift in the de novo proteome accompanies pathogenesis in an Alzheimer's disease mouse model. *Commun Biol* 2021;**4**:823.
76. Ribeiro FC, Cozachenko D, Heimfarth L. *et al.* Synaptic proteasome is inhibited in Alzheimer's disease models and associates with memory impairment in mice. *Commun Biol* 2023;**6**:1127.
77. Chocron ES, Munkácsy E, Kim HS. *et al.* Genetic and pharmacologic proteasome augmentation ameliorates Alzheimer's-like pathology in mouse and fly APP overexpression models. *Sci Adv* 2022;**8**:eabk2252.

78. Hu Y, Meuret C, Martinez A. et al. Distinct patterns of apolipoprotein C-I, C-II, and C-III isoforms are associated with markers of Alzheimer's disease. *J Lipid Res* 2021;**62**:100014.
79. Morton AM, Koch M, Mendivil CO. et al. Apolipoproteins E and CIII interact to regulate HDL metabolism and coronary heart disease risk. *JCI Insight* 2018;**3**:e98045.
80. Strittmatter WJ, Saunders AM, Schmechel D. et al. Apolipoprotein E: high-avidity binding to beta-amyloid and increased frequency of type 4 allele in late-onset familial Alzheimer disease. *PNAS* 1993;**90**:1977–1981.
81. Harold D, Abraham R, Hollingworth P. et al. Genome-wide association study identifies variants at CLU and PICALM associated with Alzheimer's disease. *Nat Genet* 2009;**41**:1088–1093.
82. Miyashita A, Koike A, Jun G. et al. SORL1 is genetically associated with late-onset Alzheimer's disease in Japanese, Koreans and Caucasians. *PLoS One* 2013;**8**:e58618.
83. Wang S, Mustafa M, Yuede CM. et al. Anti-human TREM2 induces microglia proliferation and reduces pathology in an Alzheimer's disease model. *J Exp Med* 2020;**217**:e20200785.
84. Olah M, Menon V, Habib N. et al. Single cell RNA sequencing of human microglia uncovers a subset associated with Alzheimer's disease. *Nat Commun* 2020;**11**:6129.
85. Hansen DV, Hanson JE, Sheng M. Microglia in Alzheimer's disease. *J Cell Biol* 2018;**217**:459–472.
86. Lambert J-C, Heath S, Even G. et al. Genome-wide association study identifies variants at CLU and CR1 associated with Alzheimer's disease. *Nat Genet* 2009;**41**:1094–1099.
87. Raj T, Rothamel K, Mostafavi S. et al. Polarization of the effects of autoimmune and neurodegenerative risk alleles in leukocytes. *Science* 2014;**344**:519–523.
88. Chan G, White CC, Winn PA. et al. CD33 modulates TREM2: convergence of Alzheimer loci. *Nat Neurosci* 2015;**18**:1556–1558.
89. Sayers EW, Bolton EE, Brister JR. et al. Database resources of the national center for biotechnology information. *Nucleic Acids Res* 2022;**50**:D20–D26.
90. Pekarek BT, Kochukov M, Lozzi B. et al. Oxytocin signaling is necessary for synaptic maturation of adult-born neurons. *Genes Dev* 2022;**36**:1100–1118.
91. Rio DC, Ares M, Hannon GJ. et al. Purification of RNA using TRIzol (TRI reagent). *Cold Spring Harb Protoc* 2010;**2010**:pdb.prot5439.
92. Schmittgen TD, Livak KJ. Analyzing real-time PCR data by the comparative CT method. *Nat Protoc* 2008;**3**:1101–1108.
93. Garcia I, Bhullar PK, Tepe B. et al. Local corticotropin releasing hormone (CRH) signals to its receptor CRHR1 during postnatal development of the mouse olfactory bulb. *Brain Struct Funct* 2016;**221**:1–20.
94. Beaudoin GMJ, Lee SH, Singh D. et al. Culturing pyramidal neurons from the early postnatal mouse hippocampus and cortex. *Nat Protoc* 2012;**7**:1741–1754.
95. Platt RJ, Chen S, Zhou Y. et al. CRISPR-Cas9 knockin mice for genome editing and cancer modeling. *Cell* 2014;**159**:440–455.
96. Walf AA, Frye CA. The use of the elevated plus maze as an assay of anxiety-related behavior in rodents. *Nat Protoc* 2007;**2**:322–328.
97. Kraeuter A-K, Guest PC, Sarnyai Z. The Y-maze for assessment of spatial working and reference memory in mice. *Methods Mol Biol* 2019;**1916**:105–111.
98. Samaco RC, Fryer JD, Ren J. et al. A partial loss of function allele of methyl-CpG-binding protein 2 predicts a human neurodevelopmental syndrome. *Hum Mol Genet* 2008;**17**:1718–1727.
99. Ballinger EC, Schaaf CP, Patel AJ. et al. *Mecp2* deletion from cholinergic neurons selectively impairs recognition memory and disrupts cholinergic modulation of the Perirhinal cortex. *eNeuro* 2019;**6**:ENEURO.0134–ENEURO.2019.
100. Lueptow LM. Novel object recognition test for the investigation of learning and memory in mice. *J Vis Exp* 2017; e55718.
101. Pitcher MR, Herrera JA, Buffington SA. et al. Rett syndrome like phenotypes in the R255X *Mecp2* mutant mouse are rescued by MECP2 transgene. *Hum Mol Genet* 2015;**24**:2662–2672.
102. Johnson ECB, Carter EK, Dammer EB. et al. Large-scale deep multi-layer analysis of Alzheimer's disease brain reveals strong proteomic disease-related changes not observed at the RNA level. *Nat Neurosci* 2022;**25**:213–225.
103. Raudvere U, Kolberg L, Kuzmin I. et al. g:Profiler: a web server for functional enrichment analysis and conversions of gene lists (2019 update). *Nucleic Acids Res* 2019;**47**:W191–W198.
104. Koopmans F, van Nierop P, Andres-Alonso M. et al. SynGO: an evidence-based, expert-curated Knowledge Base for the synapse. *Neuron* 2019;**103**:217–234.e4.